

Single slepton production associated with a top quark at LHC in NLO QCD

Li Xiao-Peng¹, Guo Lei¹, Ma Wen-Gan¹, Han Liang¹,
Zhang Ren-You¹, and Wang Shao-Ming^{1,2}

¹ Department of Modern Physics, University of Science and Technology
of China (USTC), Hefei, Anhui 230026, P.R.China

² Department of Physics, Chongqing University, Chongqing 401331, P.R. China

Abstract

Single slepton production in association with a top quark at the CERN Large Hadron Collider (LHC) is one of the important processes in probing the R-parity violation couplings. We calculate the QCD next-to-leading order (NLO) corrections to the $pp \rightarrow t\tilde{\ell}^- (\bar{t}\tilde{\ell}^+) + X$ process at the LHC and discuss the impacts of the QCD corrections on kinematic distributions. We investigate the dependence of the leading order (LO) and the NLO QCD corrected integrated cross section on the factorization/renormalization energy scale, slepton, stop-quark and gluino masses. We find that the uncertainty of the LO cross section due to the energy scale is obviously improved by the NLO QCD corrections, and the exclusive jet event selection scheme keeps the convergence of the perturbative series better than the inclusive scheme. The results show that the polarization asymmetry of the top-quark will be reduced by the NLO QCD corrections, and the QCD corrections generally increase with the increment of the \tilde{t}_1 or \tilde{g} mass value.

PACS: 14.65.Ha, 12.60.Jv, 12.38.Bx

I. Introduction

Supersymmetry (SUSY) is one of the most appealing theories as an extension of the standard model (SM). It provides an elegant way to solve the gauge hierarchy problem and cancel the quadratic divergences of the radiative correction to the Higgs boson mass. The minimal supersymmetric standard model (MSSM) contains SM particles, their superpartners and an additional Higgs doublet. In order to avoid the rapid proton decay, a discrete R -parity symmetry [1, 2] is introduced in the MSSM, which implies a conserved quantum number, $R_p = (-1)^{3B+L+2S}$, with B , L and S being baryon number, lepton number and spin of the particle, respectively. For all the SM particles R_p is equal to +1, while for all the superpartners R_p is -1 . So this symmetry leads to the result that the superpartners can only be produced in a pair and the lightest SUSY particle (LSP) is stable. However, such a stringent symmetry appears to be a theoretical basis; especially, we know that a stable proton can survive by imposing either L - or B -conservation [3]. At the same time, there is not enough experimental evidence for R -parity conservation, so R -parity conservation is not necessary in the MSSM. Moreover, non-zero R -parity violating (RPV) couplings could provide small neutrino masses, which could explain the phenomena of neutrino oscillation experiments. Thus, there are strong theoretical and phenomenological motivations to introduce partial R -parity violation into the most general representation of superpotential with the respect to the renormalizability and preservation of the gauge symmetries of SM and supersymmetry, which can be written as [4–6]

$$\mathcal{W}_{\hat{R}_p} = \frac{1}{2}\epsilon_{ab}\lambda_{ijk}\hat{L}_i^a\hat{L}_j^b\hat{E}_k + \epsilon_{ab}\lambda'_{ijk}\hat{L}_i^a\hat{Q}_j^b\hat{D}_k + \frac{1}{2}\epsilon_{\alpha\beta\gamma}\lambda''_{ijk}\hat{U}_i^\alpha\hat{D}_j^\beta\hat{D}_k^\gamma + \epsilon_{ab}\mu_i\hat{L}_i^a\hat{H}_2^b, \quad (1.1)$$

where i, j, k denote generation indices, a, b ($= 1, 2$) are SU(2) isospin indices, and α, β, γ are SU(3) color indices. \hat{L}_i (\hat{Q}_i) are the left-handed leptons (quarks) SU(2)-doublet chiral superfields, and \hat{E}_i (\hat{U}_i, \hat{D}_i) are the right-handed leptons (up- and down-type quarks) SU(2)-singlet chiral superfields. $H_{1,2}$ are the Higgs chiral superfields. The λ_{ijk} , λ'_{ijk} and μ_i are the dimensionless L -violating coupling coefficients, and λ''_{ijk} are the B -violating dimensionless coupling constants. As mentioned above, B and L cannot be violated at the same time. In this paper we concentrate ourselves only on the L -violating couplings, where the coefficients λ'_{ijk}

may be assumed to be non-zero.

The LHC can be used as a top-factory, and it is advantageous to study the production and decay of top quark. We suspect that the processes related with top quark can be used to probe the new physics effects since the top mass is close to the weak scale [7], particularly in the single top-quark production process the chiral structure of the interaction of the top quark may impact the polarization observable of the final top quark [8]. Therefore, the predictions including higher order corrections to single top-quark production within and beyond the SM are very important in exploring the new physics.

The single charged slepton production in association with a top quark at hadron collider is induced by the non-zero term $\lambda'_{i3k} \hat{L}_i \hat{Q}_3 \hat{D}_k$ in Eq.(1.1). The $pp \rightarrow t\tilde{\ell}_i^- (\bar{t}\tilde{\ell}_i^+) + X$ process at the LHC receives the contributions from the partonic processes $gd_k(g\bar{d}_k) \rightarrow t\tilde{\ell}_i^- (\bar{t}\tilde{\ell}_i^+)$, where i and k are the generation indices. The second term in Eq.(1.1) is related to the Born process $pp \rightarrow t\tilde{\ell}_i^- (\bar{t}\tilde{\ell}_i^+) + X$, which can be expressed as

$$\begin{aligned} \mathcal{L}_{LQD} = & \lambda'_{ijk} \left[\tilde{\nu}_{iL} \bar{d}_{kR} d_{jL} + \tilde{d}_{jL} \bar{d}_{kR} \nu_{iL} + \tilde{d}_{kR}^* \overline{\nu_{iL}^c} d_{jL} \right. \\ & \left. - \tilde{\ell}_{iL} \bar{d}_{kR} u_{jL} - \tilde{u}_{jL} \bar{d}_{kR} \ell_{iL} - \tilde{d}_{kR}^* \overline{\ell_{iL}^c} u_{jL} \right] + \text{h.c.} \end{aligned} \quad (1.2)$$

For the NLO QCD calculations, the interaction vertices of two squarks and a slepton may be involved, which can be extracted from the general soft SUSY-breaking Lagrangian [9]

$$\mathcal{L}_{\tilde{q}\tilde{q}}^{soft} = -\lambda'_{ijk} A \left(\tilde{\nu}_i \tilde{d}_{jL} \tilde{d}_{kR}^* - \tilde{\ell}_{Li} \tilde{u}_{jL} \tilde{d}_{kR}^* \right) + \text{h.c.} \quad (1.3)$$

In the above equation it is assumed that the soft breaking terms have a universal dimensionful parameter A and are proportional to the dimensionless coupling constant λ'_{ijk} . In this work we take the SUSY-breaking parameter $A = 0, \pm 1 \text{ TeV}$, separately.

The single top-quark production processes at colliders in the R -parity violating MSSM has been studied in several references [7, 10–16]. The top-quark production in association with a slepton $\tilde{\ell}_i$ at hadron collider has been studied at leading order (LO) in Refs.[17, 18], there the authors performed the signal analysis, and found that the final states in the $t\tilde{\ell}_i^- (\bar{t}\tilde{\ell}_i^+)$ production at the LHC have distinct kinematic signatures, which can be distinguished from the backgrounds.

In this paper, we present the calculations of the next-to-leading order (NLO) QCD corrections to this process. The paper is organized as follows: In section II, we present the calculations for the relevant partonic processes and parent process $pp \rightarrow t\tilde{\ell}_i^- (\bar{t}\tilde{\ell}_i^+) + X$ at the LO and QCD NLO. In section III, we give some numerical results and discussions. Finally, a short summary is given.

II. Calculations

A. LO calculation

In both the LO and NLO calculations, we apply FeynArts3.4 and FormCalc5.3 packages [19, 20] to generate Feynman diagrams, their corresponding amplitudes, and to simplify the amplitudes, separately. In Table 1 the upper 2σ bounds on λ'_{i3k} originating from Refs.[18, 21] are listed. There the coefficients $\lambda'_{i33} < \mathcal{O}(10^{-4})$ stem from assuming $m_\nu < 1eV$ and left-right mixing in the sbottom sector. Since we have the strong constraints on the λ'_{i33} coupling shown in Table 1 and the low (anti)bottom luminosity in parton distribution function (PDF) of the proton, which indicates there cannot be any significant production rates via $gb(g\bar{b}) \rightarrow t\tilde{\ell}_i^- (\bar{t}\tilde{\ell}_i^+)$ partonic processes at the LHC, we ignore their contributions in the following calculation.

λ'_{131}	$0.019 \times (m_{\tilde{t}_L}/100GeV)$	λ'_{132}	$0.28 \times (m_{\tilde{t}_L}/100GeV)$
λ'_{231}	$0.18 \times (m_{\tilde{b}_L}/100GeV)$	λ'_{232}	$0.45 (m_{\tilde{s}_R} = 100GeV)$
λ'_{331}	$0.45 (m_{\tilde{q}} = 100GeV)$	λ'_{332}	$0.45 (m_{\tilde{q}} = 100GeV)$
λ'_{i33}	$\mathcal{O}(10^{-4})$		

Table 1: Upper 2σ bounds on λ'_{i3k} , where $m_{\tilde{q}_{L(R)}}$ is the mass of the left (right) handed squark $\tilde{q}_{L(R)}$.

Due to the CP-conservation the production cross section for $gd_k \rightarrow t\tilde{\ell}_i^-$ ($i = 1, 2, 3, k = 1, 2$) subprocess is the same as that for the $g\bar{d}_k \rightarrow \bar{t}\tilde{\ell}_i^+$ ($i = 1, 2, 3, k = 1, 2$) subprocess. In this section we present only the calculations of the former subprocess. There are two tree-level Feynman diagrams contributing to the partonic process of $gd_k \rightarrow t\tilde{\ell}_i^-$ ($i = 1, 2, 3, k = 1, 2$) as shown in Fig.1(a) (for the s-channel) and Fig.1(b) (for the t-channel).

The expression of the LO cross section for the partonic process $g(p_1)d_k(p_2) \rightarrow t(p_3)\tilde{\ell}_i^-(p_4)$

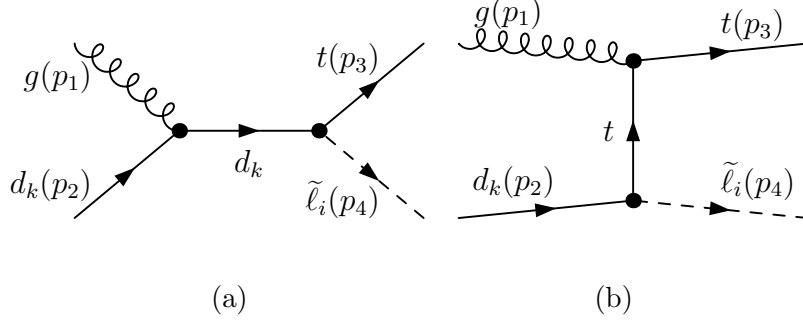


Figure 1: The tree-level Feynman diagrams of the $gd_k \rightarrow t\tilde{\ell}_i^-$ partonic process.

has the form

$$\hat{\sigma}_0(gd_k \rightarrow t\tilde{\ell}_i^-) = \frac{1}{4} \frac{1}{24} \frac{(2\pi)^4}{2\hat{s}} \int \sum_{spin}^{color} |\mathcal{M}_{LO}(gd_k \rightarrow t\tilde{\ell}_i^-)|^2 d\Omega_2, \quad (2.1)$$

where the factors $\frac{1}{4}$ and $\frac{1}{24}$ come from the averaging over the spins and colors of the initial partons, respectively, \hat{s} is the partonic center-of-mass energy squared, $\mathcal{M}_{LO}(gd_k \rightarrow t\tilde{\ell}_i^-)$ is the amplitude of the tree-level Feynman diagrams shown in Fig.1. The summation in Eq.(2.1) is taken over the spins and colors of all the relevant initial and final particles. The phase-space element $d\Omega_2$ is expressed as

$$d\Omega_2 = \delta^{(4)}(p_1 + p_2 - p_3 - p_4) \prod_{i=3,4} \frac{d^3\mathbf{p}_i}{(2\pi)^3 2E_i}. \quad (2.2)$$

The LO cross-section for the parent process $pp \rightarrow gd_k \rightarrow t\tilde{\ell}_i^- + X$ at the LHC can be obtained by performing the following integrations:

$$\sigma_{LO} = \sum_{d_k=d,s} \int_0^1 dx_1 \int_0^1 dx_2 \hat{\sigma}_0(gd_k \rightarrow t\tilde{\ell}_i^-) [G_{g/P_1}(x_1, \mu_f) G_{d_k/P_2}(x_2, \mu_f) + (x_1 \leftrightarrow x_2, P_1 \leftrightarrow P_2)], \quad (2.3)$$

where $G_{j/A}(x, \mu_f)$ is the PDF of parton j ($= g$ or d_k) in proton A ($= P_1, P_2$) which describes the probability to find a parton j with momentum xP_A in proton A , μ_f is the factorization energy scale. We adopt the CTEQ6L1 PDFs in the LO calculations.

B. Real and virtual corrections

In the NLO calculations we use the dimensional regularization method in $D = 4 - 2\epsilon$ dimensions to isolate the UV and IR singularities. Some of the virtual QCD one-loop diagrams are shown in Fig.2.

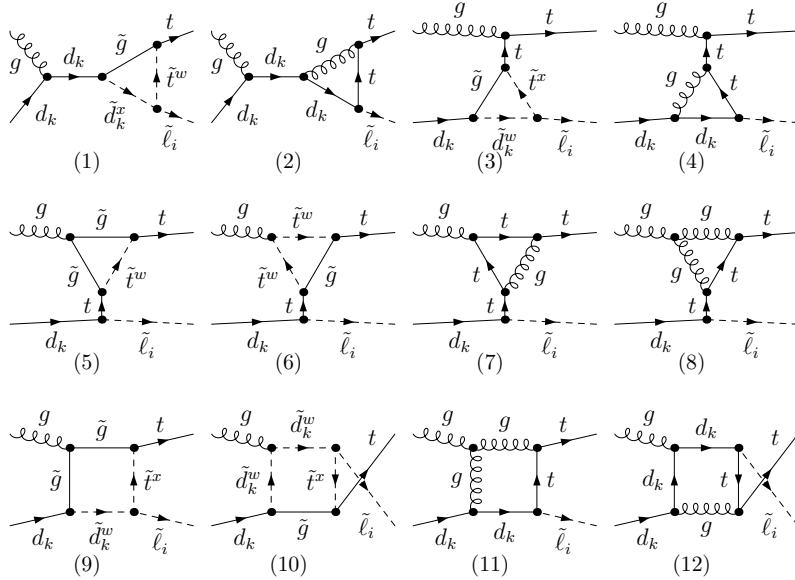


Figure 2: Some of the QCD one-loop Feynman diagrams for the $gd_k \rightarrow t\tilde{\ell}_i^-$ partonic process. The upper indices $x, w = 1, 2$, and the lower indexes i and k run from the first generation to the third generation.

The NLO QCD corrections to the $gd_k \rightarrow t\tilde{\ell}_i^-$ partonic process can be divided into two components: the virtual correction and the real radiation correction. There exist ultraviolet (UV) and infrared (IR) singularities in the virtual correction and only IR singularity in the real radiation correction. The IR singularity includes soft divergence and collinear divergence. In the virtual correction component, the UV divergence vanishes by performing renormalization procedure, and the soft IR divergency can be completely eliminated by adding the contribution from the real gluon emission partonic process $gd_k \rightarrow t\tilde{\ell}_i + g$. The collinear divergence in the virtual correction can be partially canceled by the collinear divergences in real gluon/light-(anti)quark emission processes, but there still exists residual collinear divergence which will be absorbed by the redefinitions of the PDFs.

The one-loop diagrams can be divided into two independent parts. One is the SM-like component arising from the diagrams including gluon/quark loop, another is the pure supersymmetric (pSUSY) QCD part where each diagram includes a gluino/squark loop. Correspondingly we divide the counterterms also into the SM-like QCD and the pSUSY QCD parts. The

definitions of the relevant counterterms are adopted as

$$\begin{aligned}
q_{L/R} &\rightarrow \left(1 + \frac{1}{2}\delta Z_{L/R}^q\right) q_{L/R} = \left[1 + \frac{1}{2}\left(\delta Z_{L/R}^{q,(SM-like)} + \delta Z_{L/R}^{q,(pSUSY)}\right)\right] q_{L/R} \\
G_\mu^a &\rightarrow \left(1 + \frac{1}{2}\delta Z_g\right) G_\mu^a = \left[1 + \frac{1}{2}\left(\delta Z_g^{(SM-like)} + \delta Z_g^{(pSUSY)}\right)\right] G_\mu^a \\
m_t &\rightarrow m_t + \delta m_t = m_t + \delta m_t^{(SM-like)} + \delta m_t^{(pSUSY)} \\
g_s &\rightarrow g_s + \delta g_s = g_s + \delta g_s^{(SM-like)} + \delta g_s^{(pSUSY)} \\
\lambda'_{i3k} &\rightarrow \lambda'_{i3k} + \delta\lambda'_{i3k},
\end{aligned} \tag{2.4}$$

where g_s is the strong coupling constant, $q_{L/R}$ denote the fields of top and $d_k (= d, s)$ quarks, and G_μ^a represents the gluon field. We renormalize the relevant fields and top-quark mass in the on-shell scheme [22]. For the renormalization of the QCD strong coupling constant g_s and the R -parity violating coupling coefficient λ'_{i3k} , we use the \overline{MS} scheme [23, 24]. The counterterm of the g_s can be expressed as

$$\begin{aligned}
\frac{\delta g_s^{(SM-like)}}{g_s} &= -\frac{\alpha_s(\mu_r)}{4\pi} \left[\frac{\beta_0^{(SM-like)}}{2} \frac{1}{\bar{\epsilon}} + \frac{1}{3} \ln \frac{m_t^2}{\mu_r^2} + \frac{1}{3} \ln \frac{m_b^2}{\mu_r^2} \right], \\
\frac{\delta g_s^{(pSUSY)}}{g_s} &= -\frac{\alpha_s(\mu_r)}{4\pi} \left[\frac{\beta_1^{(pSUSY)}}{2} \frac{1}{\bar{\epsilon}} + \frac{N}{3} \ln \frac{m_{\tilde{g}}^2}{\mu_r^2} + \sum_{U=u,c,t}^{i=1,2} \frac{1}{12} \ln \frac{m_{\tilde{U}_i}^2}{\mu_r^2} + \sum_{D=d,s,b}^{j=1,2} \frac{1}{12} \ln \frac{m_{\tilde{D}_j}^2}{\mu_r^2} \right],
\end{aligned} \tag{2.5}$$

where $1/\bar{\epsilon} = 1/\epsilon_{UV} - \gamma_E + \ln(4\pi)$, $\beta_0^{(SM-like)} = \frac{11}{3}N - \frac{2}{3}n_{lf} - \frac{4}{3}$ and $\beta_1^{(pSUSY)} = -\frac{2}{3}N - \frac{1}{3}(n_{lf} + 2)$ with $N = 3$ and $n_{lf} = 4$.

With the Lagrangian shown in Eq.(1.2), the counterterm of the $\tilde{\ell}_i - \bar{d}_k - t$ vertex is expressed as below:

$$\delta V_{\tilde{\ell}_i \bar{d}_k t} = -\lambda'_{i3k} \left(\frac{\delta\lambda'_{i3k}}{\lambda'_{i3k}} + \frac{1}{2}\delta Z_R^{d_k} + \frac{1}{2}\delta Z_L^t \right). \tag{2.6}$$

By using the \overline{MS} scheme to renormalize the $\tilde{\ell}_i - \bar{d}_k - t$ coupling, we get

$$\delta\lambda'_{i3k} = \lambda'_{i3k} \left(-\frac{C_F}{2} \right) \frac{\alpha_s}{\pi\bar{\epsilon}}, \tag{2.7}$$

where $C_F = 4/3$. After the renormalization we get a UV-finite virtual correction to the partonic process $gd_k \rightarrow t\tilde{\ell}_i^-$.

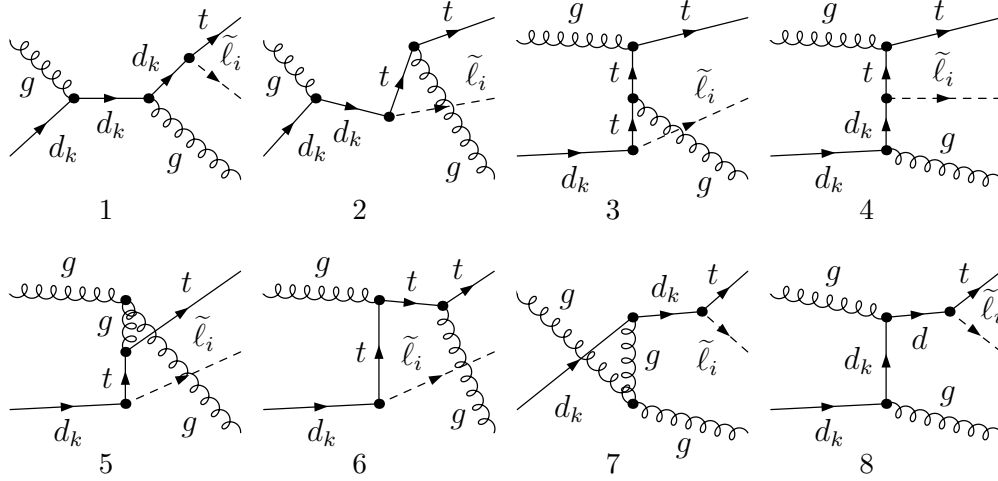


Figure 3: The tree-level Feynman diagrams for the real gluon emission process $gd_k \rightarrow t\tilde{\ell}_i^- + g$.

The real radiation correction includes the contributions from the gluon and light-(anti)-quark emission processes. The contribution of real radiation processes is at the same α_s order as the virtual correction to the partonic process $gd_k \rightarrow t\tilde{\ell}_i^-$ in perturbation theory according to the Kinoshita–Lee–Nauenberg(KLN) theorem [25, 26]. The tree-level Feynman diagrams of the real gluon emission partonic process $g(p_1)d_k(p_2) \rightarrow t(p_3)\tilde{\ell}_i^-(p_4)g(p_5)$ are depicted in Fig.3. We adopt the two cutoff phase-space slicing (TCPSS) method [27] to isolate the IR singularities for the real emission subprocesses by introducing two cutoff parameters δ_s and δ_c . The arbitrary small soft cutoff δ_s separates the three-body final state phase space of real emission subprocess into two regions: the soft region ($E_5 \leq \delta_s\sqrt{\hat{s}}/2$) and the hard region ($E_5 > \delta_s\sqrt{\hat{s}}/2$). The collinear cutoff δ_c separates hard region into the hard collinear (HC) region and hard non-collinear (\overline{HC}) region. The region for real hard gluon/light-(anti)quark emission with \hat{s}_{15} (or \hat{s}_{25}) $< \delta_c\hat{s}$ (where $\hat{s}_{ij} = (p_i + p_j)^2$) is called the HC region. Otherwise it is called the \overline{HC} region. Then the cross section of the real gluon emission partonic process can be written as

$$\hat{\sigma}_g^R(gd_k \rightarrow t\tilde{\ell}_i^-g) = \hat{\sigma}_g^S + \hat{\sigma}_g^H = \hat{\sigma}_g^S + \hat{\sigma}_g^{HC} + \hat{\sigma}_g^{\overline{HC}} \quad (2.8)$$

where $\hat{\sigma}_g^S$, $\hat{\sigma}_g^{HC}$ and $\hat{\sigma}_g^{\overline{HC}}$ are the cross sections in the soft gluon region, hard collinear region and hard non-collinear region, respectively.

The light-(anti)quark emission contribution at the QCD NLO to the $pp \rightarrow t\tilde{\ell}_i^- + X$ process includes the partonic channels: (1) $q(\bar{q})d_k \rightarrow t\tilde{\ell}_i^- + q(\bar{q})$, (2) $gg \rightarrow t\tilde{\ell}_i^- + d_k$. The corresponding

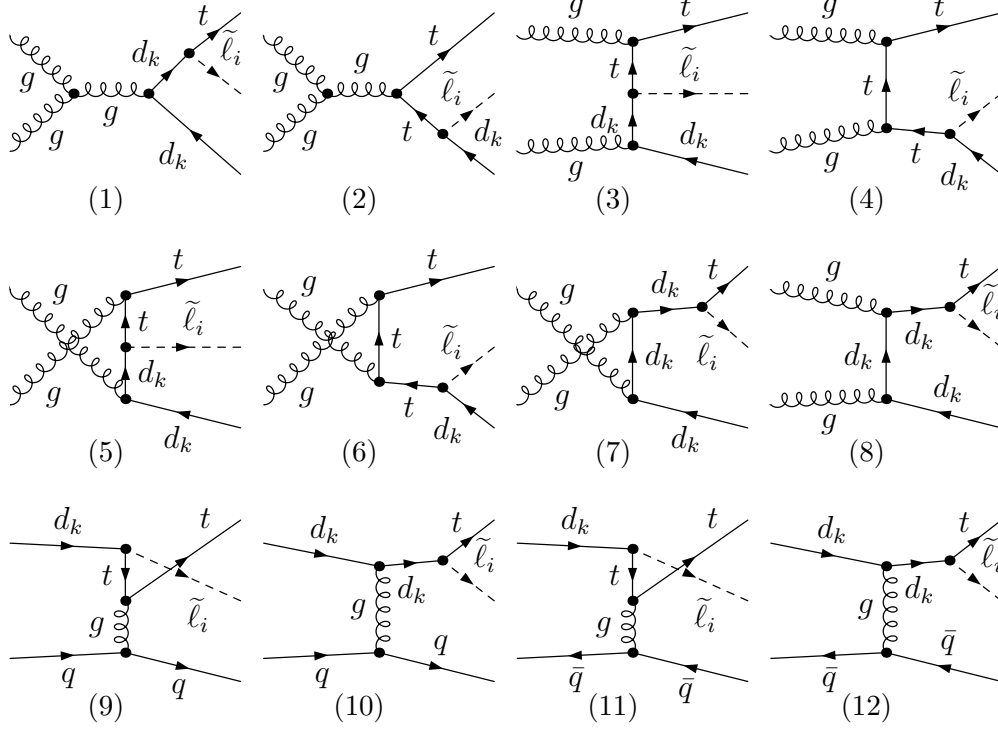


Figure 4: The tree-level Feynman diagrams for the real light-(anti)quark emission processes. (1–8), (9–10) and (11–12) are for the $gg \rightarrow t\tilde{\ell}_i^- d_k^-$, $qd_k \rightarrow t\tilde{\ell}_i^- q$ and $\bar{q}d_k \rightarrow t\tilde{\ell}_i^- \bar{q}$ ($q = u, d, s, c$) partonic processes, respectively.

Feynman diagrams of these partonic processes at the tree-level are shown in Fig.4. There the diagrams by exchanging the identical incoming quarks in Figs.4(9)-(10) for the partonic process $qd_k \rightarrow t\tilde{\ell}_i^- q$, i.e., $q = d_k (= d, s)$ are not drawn.

Again we use the TCPSS method to splitting the three-body phase space into collinear (C) and non-collinear (\bar{C}) regions, and get the cross sections for the subprocesses $gg \rightarrow t\tilde{\ell}_i^- \bar{d}_k$ and $q(\bar{q})d_k \rightarrow t\tilde{\ell}_i^- q(\bar{q})$ at the tree level expressed as

$$\hat{\sigma}^R(gg \rightarrow t\tilde{\ell}_i^- \bar{d}_k) = \hat{\sigma}_{\bar{d}_k}^R = \hat{\sigma}_{\bar{d}_k}^C + \hat{\sigma}_{\bar{d}_k}^{\bar{C}}, \quad (2.9)$$

$$\hat{\sigma}^R(q(\bar{q})d_k \rightarrow t\tilde{\ell}_i^- q(\bar{q})) = \hat{\sigma}_{q(\bar{q})}^R = \hat{\sigma}_{q(\bar{q})}^C + \hat{\sigma}_{q(\bar{q})}^{\bar{C}}. \quad (2.10)$$

The cross-sections in the non-collinear region, $\hat{\sigma}_{\bar{d}_k}^{\bar{C}}$, $\hat{\sigma}_{q(\bar{q})}^{\bar{C}}$ (in Eqs.(2.9), (2.10)) and $\hat{\sigma}_g^{\bar{H}\bar{C}}$ (in Eq.(2.8)), are finite and can be evaluated in four dimensions by using the general Monte Carlo method. After summing all the contributions mentioned above there still exists the remaining collinear divergence, which will be absorbed by the redefinition of the PDFs at the NLO.

C. Total NLO QCD correction

Given the NLO correction components to the cross sections of the subprocesses above, the full NLO QCD correction to the cross section for the $pp \rightarrow t\tilde{\ell}_i^- + X$ process at the LHC is formally given by the QCD factorization formula as

$$\begin{aligned} & \sigma_{NLO}(pp \rightarrow t\tilde{\ell}_i^- + X) \\ = & \sum_{(jk)} \int_0^1 dx_1 \int_0^1 dx_2 \{ [G_{j/P_1}(x_1, \mu_f) G_{k/P_2}(x_2, \mu_f) \hat{\sigma}_{(jk)}(x_1 x_2 s)] + (x_1 \leftrightarrow x_2, P_1 \leftrightarrow P_2) \}, \end{aligned} \quad (2.11)$$

where j and k sum over all possible types of initial partons contributing to the subprocesses up to the QCD NLO, i.e., (jk) represents (gd) , (gs) , (gg) , (qd) , (qs) , $(\bar{q}d)$ and $(\bar{q}s)$ (where $q = u, d, c, s$). We consistently adopt the CTEQ6m PDFs[28, 29] for $G_{j/P_1(P_2)}(x_1, \mu_f)$ and $G_{k/P_2(P_1)}(x_2, \mu_f)$. The total NLO QCD correction $\Delta\sigma_{NLO}$ to the $pp \rightarrow t\tilde{\ell}_i^- + X$ process can be divided into two-body term and three-body term, i.e., $\Delta\sigma_{NLO} = \Delta\sigma^{(2)} + \Delta\sigma^{(3)}$. The two-body term consists of the virtual correction and the cross section for the real gluon/light-(anti)quark emission process in the soft and hard collinear phase-space region. The three-body term consists of the cross section for the real gluon/light-(anti)quark emission process in the hard non-collinear phase space. Finally, the QCD corrected total cross section for the $pp \rightarrow t\tilde{\ell}_i^- + X$ process is

$$\sigma_{NLO} = \sigma_{LO} + \sigma^{(2)} + \sigma^{(3)}. \quad (2.12)$$

III. Numerical results and discussion

In this section we present and discuss the numerical results for the LO and NLO QCD corrected cross sections for the $pp \rightarrow t\tilde{\ell}_i^-(\bar{t}\tilde{\ell}_i^+) + X$ process at the early ($\sqrt{s} = 7 \text{ TeV}$) and future ($\sqrt{s} = 14 \text{ TeV}$) LHC. In order to check the correctness of our LO calculations, we list our LO numerical results for $pp \rightarrow g d_k \rightarrow t\tilde{\ell}_i^- + X$ process in Table 2, and compare them with those presented in Table 2 and Fig.3 of Ref.[18]. Our results are obtained by employing the same input parameters and PDFs as used in previous work [18]. We can see that they are in

$m_{\tilde{\ell}_i} (GeV)$	$pp \rightarrow t\tilde{\ell}_i^- + X$ via $\lambda'_{i31} = 0.1$		$pp \rightarrow t\tilde{\ell}_i^- + X$ via $\lambda'_{i32} = 0.1$	
	our $\sigma_{LO}(\text{fb})$	$\sigma_{LO}(\text{fb})$ in Ref.[18]	our $\sigma_{LO}(\text{fb})$	$\sigma_{LO}(\text{fb})$ in Ref.[18]
200	377.8(5)	378	73.5(4)	73.5
500	51.80(7)	52	7.64(4)	7.7
800	11.58(8)	11.6	1.370(7)	1.4

Table 2: The comparison of our LO numerical results for the $pp \rightarrow gd_k \rightarrow t\tilde{\ell}_i^- + X$ process at the $\sqrt{s} = 14 \text{ TeV}$ LHC with those in Ref.[18]. The relevant parameters and the PDFs being the same as used in Ref.[18].

agreement. But we should say that most of the data taken from Ref.[18] are read from the figure with large errors.

In the following numerical calculation, we take one-loop running α_s and two-loop running α_s in the LO and NLO calculations, respectively [30]. The number of active flavors is taken as $N_f = 4$, and the QCD parameter $\Lambda_4^{LO} = 215 \text{ MeV}$ and the CTEQ6L1 PDFs are adopted in the LO calculation, while $\Lambda_4^{\overline{MS}} = 326 \text{ MeV}$ and the CTEQ6M PDFs are used for the NLO calculation [28, 29]. We set factorization scale and renormalization scale equal and take $\mu = \mu_0 \equiv (m_t + m_{\tilde{\ell}_i})/2$ in default. The CKM matrix is set to the unit matrix. We ignore the masses of electron and u-, d-, s-, c-quarks, and take $m_t = 172.0 \text{ GeV}$ and $m_b = 4.2 \text{ GeV}$ in the numerical calculation [30].

In the calculation of the process $pp \rightarrow t\tilde{\ell}_i^- + X$ we assume that the masses of the sleptons of three generations are degenerated with the values of $m_{\tilde{\ell}_i} = m_{\tilde{\ell}_L}$, ($i = 1, 2, 3$), and take the \hat{R}_p coupling parameters as (1) $\lambda'_{i31} = 0.1$ and the other $\lambda' = 0$; (2) $\lambda'_{i32} = 0.1$ and the other $\lambda' = 0$. We follow the SPA benchmark point SPS1a' [31], where the input parameters are $m_0 = 70 \text{ GeV}$, $m_{1/2} = 250 \text{ GeV}$, $A_0 = -300 \text{ GeV}$, $sign(\mu) = +1$, $\tan\beta = 10$, and $m_t = 172.0 \text{ GeV}$, but we assume that there is no left- and right-squark mixing in the first two generations and the degenerated sleptons having the masses $m_{\tilde{\ell}_i} = 189.9 \text{ GeV}$ ($i = 1, 2, 3$). Then we get the left-right stop (sbottom) mixing angle $\theta_t = 57.026^\circ$ ($\theta_b = 19.75^\circ$) by adopting the ISAJET program[32], and the other relevant SUSY parameters with the values:

$$\begin{aligned}
m_{\tilde{g}} &= 607.1 \text{ GeV}, & m_{\tilde{t}_1} &= 366.5 \text{ GeV}, & m_{\tilde{t}_2} &= 585.5 \text{ GeV}, \\
m_{\tilde{b}_1} &= 506.3 \text{ GeV}, & m_{\tilde{b}_2} &= 545.7 \text{ GeV}, & m_{\tilde{u}_1} &= m_{\tilde{c}_1} = m_{\tilde{u}_R} = 547.2 \text{ GeV},
\end{aligned}$$

$$\begin{aligned}
m_{\tilde{u}_2} &= m_{\tilde{c}_2} = m_{\tilde{u}_L} = 564.7 \text{ GeV}, & m_{\tilde{d}_1} &= m_{\tilde{s}_1} = m_{\tilde{d}_R} = 546.9 \text{ GeV}, \\
m_{\tilde{d}_2} &= m_{\tilde{s}_2} = m_{\tilde{d}_L} = 570.1 \text{ GeV}, & m_{\tilde{\chi}_1^0} &= 97.7 \text{ GeV}, & \mu &= 396 \text{ GeV}.
\end{aligned}
\tag{3.1}$$

The SM parameters used in the calculation are taken as follows [30]

$$\begin{aligned}
\alpha_{ew} &= 1/137.036, & \sin^2 \theta_w &= 0.23119, & m_W &= 80.398 \text{ GeV}, \\
m_Z &= 91.1876 \text{ GeV}, & m_\mu &= 0.1057 \text{ GeV}.
\end{aligned}
\tag{3.2}$$

In the following calculations we take the parameters stated above if there is no other statement.

The independence of the full NLO QCD correction on the two cutoffs, δ_s and δ_c , is confirmed numerically. Figs.5(a,b) demonstrate that the total NLO QCD correction to the $pp \rightarrow gd \rightarrow t\tilde{\ell}_i^- + X$ process with $A = 0 \text{ TeV}$ at the $\sqrt{s} = 14 \text{ TeV}$ LHC does not depend on the arbitrarily chosen values of the δ_s and δ_c within the calculation errors, where we take $\lambda'_{i31} = 0.1$ and other $\lambda' = 0$. In Fig.5(a), the two-body correction $\Delta\sigma^{(2)}$, three-body correction $\Delta\sigma^{(3)}$ and the total QCD correction ($\Delta\sigma_{NLO}$) for the $pp \rightarrow gd \rightarrow t\tilde{\ell}_i^- + X$ process are depicted as functions of the soft cutoff δ_s running from 1×10^{-5} to 1×10^{-3} with $\delta_c = \delta_s/50$. In Fig.5(b), the amplified curve for $\Delta\sigma_{NLO}$ is depicted. The results in these two figures demonstrate that the total QCD correction to the $pp \rightarrow gd \rightarrow t\tilde{\ell}_i^- + X$ process is independent of δ_s and δ_c . It verifies the cancelation of the soft/collinear IR divergence in the total QCD correction to $pp \rightarrow gd \rightarrow t\tilde{\ell}_i^- + X$. In further numerical calculations, we fix $\delta_s = 5 \times 10^{-5}$ and $\delta_c = \delta_s/50$.

For the gluon/light-(anti)quark jet event selection we adopt two selection schemes: (1) Inclusive jet event selection scheme. With this scheme we accept all the real gluon/light-(anti)quark emission events. (2) Exclusive jet event selection scheme, by which we accept the real gluon/light-(anti)quark emission event satisfying the restriction of either $p_T^{jet} < p_{T,jet}^{cut}$ on the jet transverse momentum or $\eta^{jet} > \eta_{jet}^{cut}$ on the jet rapidity. In further calculations with exclusive jet event selection scheme, we take the cut parameters for gluon/light-(anti)quark jet as $p_{T,jet}^{cut} = 50 \text{ GeV}$ and $\eta_{jet}^{cut} = 3$.

One of the main reasons to base the LHC analyses on higher order predictions is the stabilization of the dependence on the unphysical renormalization and the factorization scales. In the upper figures of Figs.6(a,b,c), we show the dependence of the LO and NLO QCD corrected cross

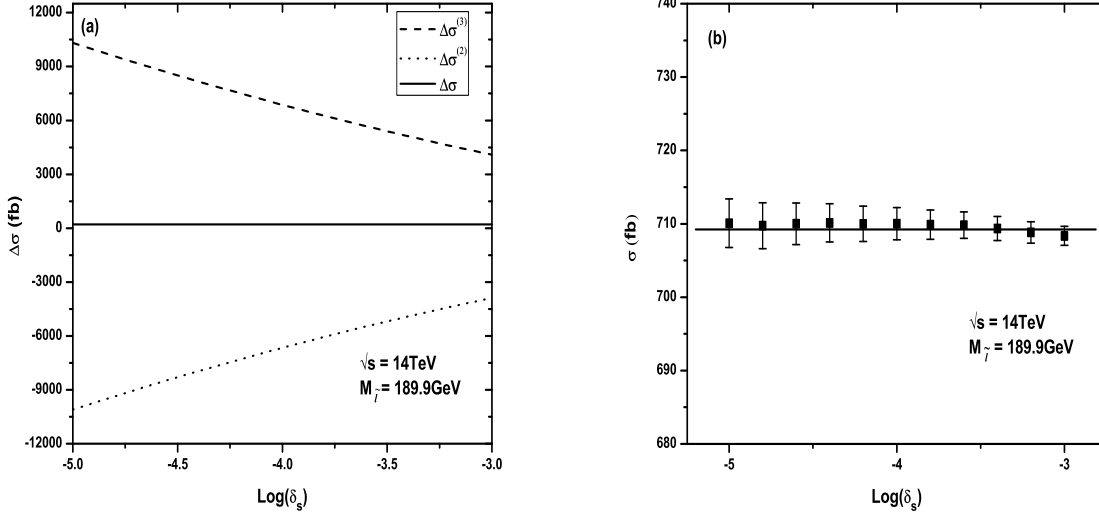


Figure 5: (a) The dependence of NLO QCD corrections to the $pp \rightarrow gd \rightarrow t\tilde{\ell}_i^- + X$ process on the soft cutoff δ_s at the $\sqrt{s} = 14 \text{ TeV}$ LHC with $A = 0 \text{ TeV}$, $m_{\tilde{\ell}_i} = 189.9 \text{ GeV}$ and $\delta_c = \delta_s/50$. (b) The NLO QCD corrected total cross section σ_{NLO} with calculation errors as the function of δ_s .

sections for the processes $pp \rightarrow gd \rightarrow t\tilde{\ell}_i^- + X$, $pp \rightarrow g\bar{d} \rightarrow \bar{t}\tilde{\ell}_i^+ + X$, and $pp \rightarrow gs \rightarrow t\tilde{\ell}_i^- + X$ on the factorization/renormalization scale (μ/μ_0) with $A = 0 \text{ TeV}$ at the $\sqrt{s} = 7 \text{ TeV}$ and $\sqrt{s} = 14 \text{ TeV}$ LHC, respectively. The corresponding K-factor [$K \equiv \sigma_{NLO}/\sigma_{LO}$] are shown in the lower figures of Figs.6(a,b,c). Since the luminosities of the s - and \bar{s} -quark in proton are the same, the observables for the process $pp \rightarrow g\bar{s} \rightarrow \bar{t}\tilde{\ell}_i^+ + X$ are equal to those for the process $pp \rightarrow gs \rightarrow t\tilde{\ell}_i^- + X$, we present only the plots for the process $pp \rightarrow gs \rightarrow t\tilde{\ell}_i^- + X$. There we assume $\mu \equiv \mu_r = \mu_f$ for simplicity, and set $\lambda'_{i31} = 0.1$ and other $\lambda' = 0$ in Figs.6(a,b), while $\lambda'_{i32} = 0.1$ and other $\lambda' = 0$ in Fig.6(c). The curves labeled NLO(I) (NLO(II)) denotes the NLO QCD corrected cross section with the inclusive (exclusive) jet events selection scheme. The curves in the lower figures of Figs.6(a,b,c) labeled (i), (ii), (iii) and (iv) correspond to the K-factors for (i) the inclusive scheme with $\sqrt{s} = 14 \text{ TeV}$, (ii) the inclusive scheme with $\sqrt{s} = 7 \text{ TeV}$, (iii) the exclusive scheme with $\sqrt{s} = 14 \text{ TeV}$, (iv) the exclusive scheme with $\sqrt{s} = 7 \text{ TeV}$, respectively. These notations are also adopted in the following figures. We can see from Figs.6(a,b,c) when the scale μ runs from $0.1\mu_0$ to $4\mu_0$, the curves for the NLO QCD

corrected cross section becomes more stable in comparison with the corresponding curves for the LO. It demonstrates that the NLO QCD corrections can improve the scale uncertainty apparently, and the exclusive scheme keeps the convergence of the perturbative series better than the inclusive scheme in the plotted μ/μ_0 range.

In Figs.7(a,b,c) we plot the LO, NLO QCD corrected cross sections and the corresponding K-factors as the functions of the final slepton mass $m_{\tilde{\ell}_i}$ with $A = 0 \text{ TeV}$ for the $pp \rightarrow gd \rightarrow t\tilde{\ell}_i^- + X$, $pp \rightarrow g\bar{d} \rightarrow \bar{t}\tilde{\ell}_i^+ + X$, and $pp \rightarrow gs \rightarrow t\tilde{\ell}_i^- + X$ processes, respectively. In each figure the curves for the $\sqrt{s} = 7 \text{ TeV}$ and $\sqrt{s} = 14 \text{ TeV}$ LHC are depicted. In Figs.7(a,b) we set the R -parity violating coupling coefficients as $\lambda'_{i31} = 0.1$ and the other $\lambda' = 0$, while in Fig.7(c) we have $\lambda'_{i32} = 0.1$ and the other $\lambda' = 0$. We can see that both the LO and NLO QCD corrected cross sections decrease with the increment of the value of $m_{\tilde{\ell}_i}$. The curves in these figures show that the cross sections for $t\tilde{\ell}_i^-$ and $\bar{t}\tilde{\ell}_i^+$ production processes are different. Unlike the luminosities of s - and \bar{s} -quark in proton, being equal, the initial d-quark has a higher luminosity than the \bar{d} -quark. This induces the cross-section of the process $pp \rightarrow gd \rightarrow t\tilde{\ell}_i^- + X$ to always be larger than the process $pp \rightarrow g\bar{d} \rightarrow \bar{t}\tilde{\ell}_i^+ + X$.

The SUSY partners \tilde{t}_1 and \tilde{g} appear only at one-loop level (shown in Fig.2). We show the virtual influences of $m_{\tilde{t}_1}$ and $m_{\tilde{g}}$ on the NLO QCD corrections by taking three different values of the SUSY-breaking parameter A (i.e., $A = 0 \text{ TeV}$ and $\pm 1 \text{ TeV}$) in Figs.8–10 and Figs.11–13, separately. Figs.8–10(a,b,c) (Figs.11–13(a,b,c)) show the NLO QCD corrections ($\Delta\sigma_{NLO}$) and the corresponding K-factors as functions of $m_{\tilde{t}_1}$ ($m_{\tilde{g}}$) for the $pp \rightarrow gd \rightarrow t\tilde{\ell}_i^- + X$, $pp \rightarrow g\bar{d} \rightarrow \bar{t}\tilde{\ell}_i^+ + X$, and $pp \rightarrow gs \rightarrow t\tilde{\ell}_i^- + X$ processes with $A = 0 \text{ TeV}$ and $\pm 1 \text{ TeV}$ at the early and future LHC, respectively. There we adopt both the inclusive and exclusive schemes in the NLO calculations. In Figs.8–13(a,b) we set $\lambda'_{i31} = 0.1$ and the other $\lambda' = 0$, while in Fig.8–13(c) we take $\lambda'_{i32} = 0.1$ and the other $\lambda' = 0$. In those figures most of the curves for the NLO QCD corrections and the corresponding K-factors always increase with the increment of $m_{\tilde{t}_1}$ ($m_{\tilde{g}}$) except those $\Delta\sigma_{NLO}$ curves in Fig.10(c) and the curves in the region of $m_{\tilde{g}} < 200 \text{ GeV}$ in Figs.13(a,b,c). It shows that the NLO SUSY QCD corrections to these processes generally increase in the large $m_{\tilde{t}_1}$ or $m_{\tilde{g}}$ region. That is because the SUSY QCD correction coming

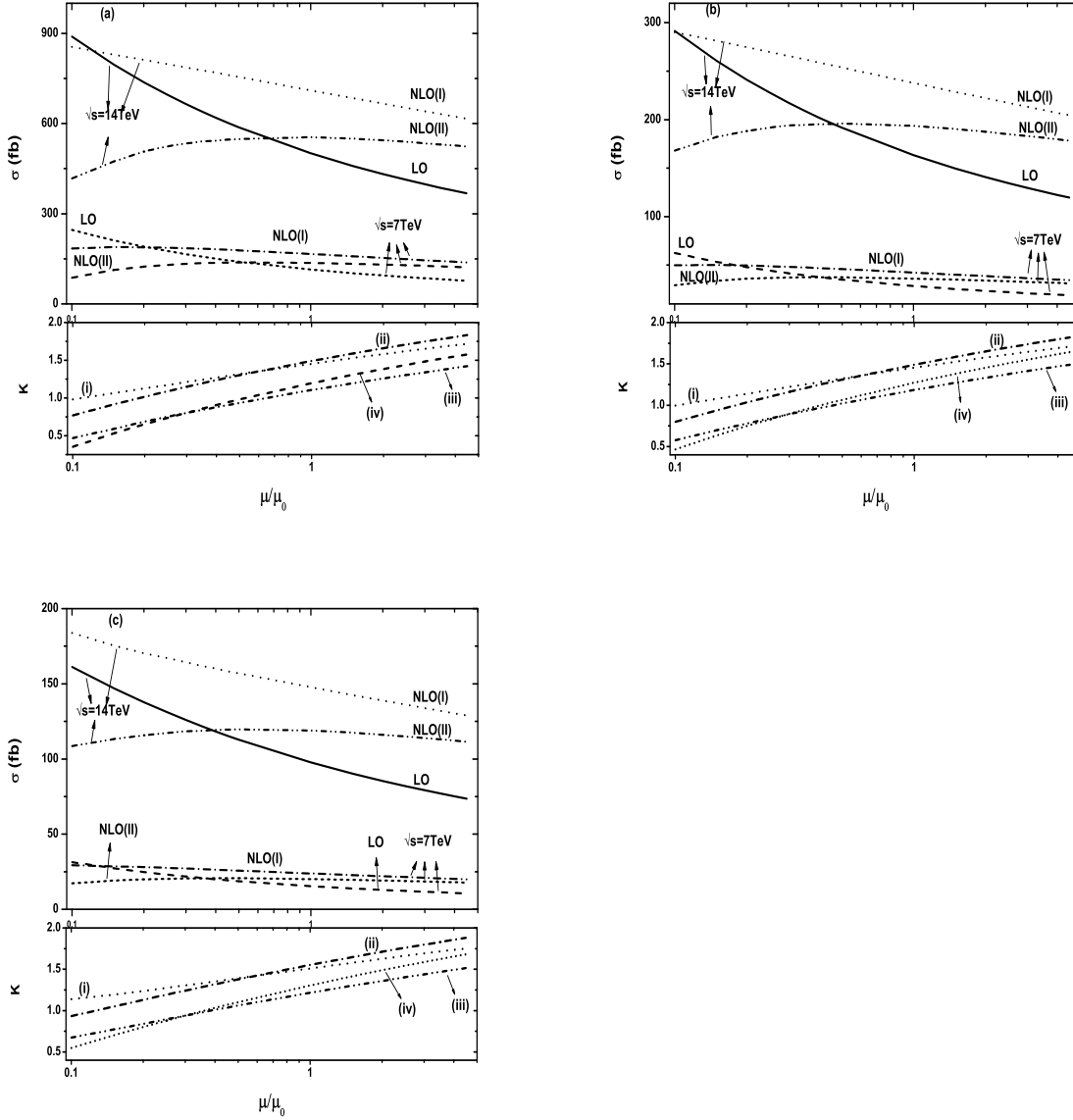


Figure 6: The LO, NLO QCD corrected cross sections and the corresponding K-factors versus the factorization/renormalization scale (μ/μ_0) with $A = 0 \text{ TeV}$ at the LHC. (a) For the $pp \rightarrow g\bar{d} \rightarrow t\tilde{\ell}_i^- + X$ process. (b) For the $pp \rightarrow g\bar{d} \rightarrow t\tilde{\ell}_i^+ + X$ process. (c) For the $pp \rightarrow gs \rightarrow t\tilde{\ell}_i^- + X$ process. The K-factor curves labeled (i), (ii), (iii) and (iv) are for (i) the inclusive scheme with $\sqrt{s} = 14 \text{ TeV}$, (ii) the inclusive scheme with $\sqrt{s} = 7 \text{ TeV}$, (iii) the exclusive scheme with $\sqrt{s} = 14 \text{ TeV}$, (iv) the exclusive scheme with $\sqrt{s} = 7 \text{ TeV}$, respectively.

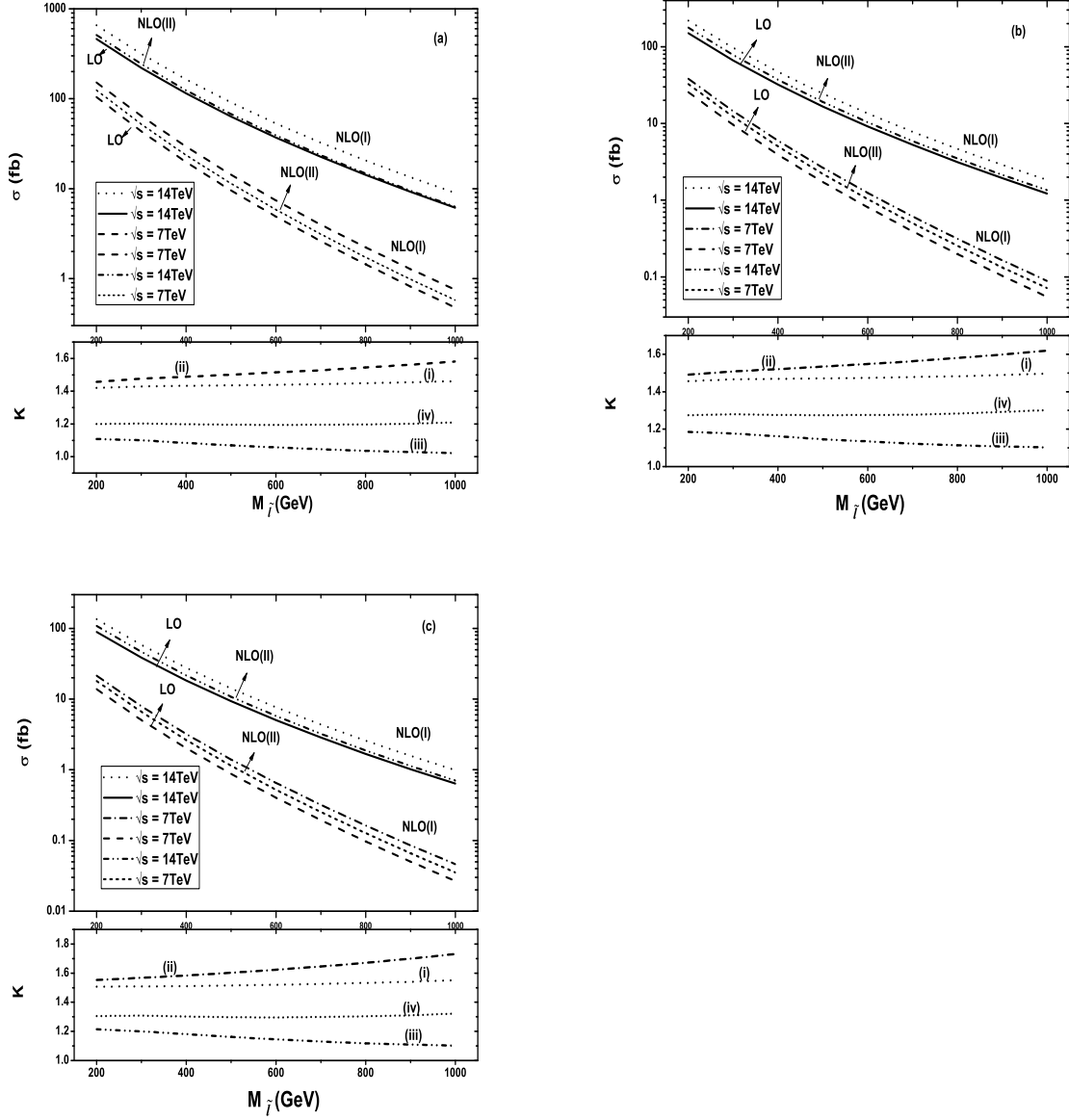


Figure 7: The LO, NLO QCD corrected cross sections and the corresponding K-factors versus the mass of slepton $m_{\tilde{\ell}_i}$ with $A = 0$ TeV at the LHC. (a) For the $pp \rightarrow gd \rightarrow t\tilde{\ell}_i^- + X$ process. (b) For the $pp \rightarrow g\bar{d} \rightarrow t\tilde{\ell}_i^+ + X$ process. (c) For the $pp \rightarrow gs \rightarrow t\tilde{\ell}_i^- + X$ process. The descriptions for the K-factor curves labeled (i), (ii), (iii) and (iv) are the same as in Figs.6.

from the renormalization counterterm of the amplitude $\delta\mathcal{M}$ involves the logarithm terms of $\ln\left(\frac{m_{\tilde{t}_1}^2}{\mu_r^2}\right)$ and $\ln\left(\frac{m_{\tilde{g}}^2}{\mu_r^2}\right)$ at the SUSY QCD one-loop level. The logarithm term contributions can be absorbed by a redefinition of the coupling λ' [33]. In this work we do not need to adopt this decoupling scheme, since in our consideration we take the squark and gluino mass quantitatively at the same order as the scale μ .

Figs.8 and Figs.11 show that if we take $A = 0$, the NLO QCD corrections are still related to $m_{\tilde{t}_1}$ and $m_{\tilde{g}}$. This can be understood from the fact that the NLO QCD contributions from the counterterms shown in Eqs.(2.4)–(2.5) and the loop diagrams such as Figs.2(5,6), are relevant to the masses of \tilde{t} and \tilde{g} . We can also see the $\Delta\sigma_{NLO}$ curves versus $m_{\tilde{t}_1}$ in Fig.10(c) for the $pp \rightarrow gs \rightarrow t\tilde{\ell}_i^- + X$ process, and the $\Delta\sigma_{NLO}$ curves in the region around $m_{\tilde{g}} \sim 200 \text{ GeV}$ in Figs.13(a,b,c) are obviously distorted by the contributions from the diagrams involving the $\tilde{t}_j\text{--}\tilde{d}_k\text{--}\tilde{l}_i$ coupling with $A = 1 \text{ TeV}$. In order to understand the contributions from the non-zero $\tilde{t}_j\text{--}\tilde{d}_k\text{--}\tilde{l}_i$ coupling more clearly, we provide the plots of $\delta\sigma_{NLO}^\pm (\equiv \sigma_{NLO}(A = \pm 1 \text{ TeV}) - \sigma_{NLO}(A = 0 \text{ TeV}))$ versus the $m_{\tilde{g}}$ in Figs.14(a,b,c) for the processes $pp \rightarrow gd \rightarrow t\tilde{\ell}_i^- + X$, $pp \rightarrow g\bar{d} \rightarrow \bar{t}\tilde{\ell}_i^+ + X$ and $pp \rightarrow gs \rightarrow t\tilde{\ell}_i^- + X$, separately. There we can see that in the region of $m_{\tilde{g}} < 400 \text{ GeV}$, $\delta\sigma_{NLO}^+$ is always positive, while $\delta\sigma_{NLO}^-$ remains negative.

In the following calculations we fix the SUSY-breaking parameter $A = 0 \text{ TeV}$. We show the polarization asymmetries (A_t) of the (anti)top quark as a function of $m_{\tilde{t}_i}$ at the LO and NLO QCD for the processes $pp \rightarrow gd_k(g\bar{d}_k) \rightarrow t\tilde{\ell}_i^-(\bar{t}\tilde{\ell}_i^+) + X$ in Figs.15(a,b,c,d). A_t is defined as $A_t = \frac{N_+ - N_-}{N_+ + N_-}$, where N_+ and N_- refer to the numbers of positive and negative helicity (anti)top quarks respectively. In Ref.[17], the LO A_t at the LHC has been plotted and it shows that the LO A_t changes signs for a slepton mass of around 870–900 GeV . As we can see in Figs.15(a,b,c,d), the polarization degree of the (anti)top quark has been reduced obviously by the NLO QCD correction. That is because the NLO QCD radiation corrections destroy the chiral structure of the interaction of top quark and reduce the LO polarization asymmetry A_t . Although the cross sections for the processes $pp \rightarrow g\bar{s} \rightarrow \bar{t}\tilde{\ell}_i^+ + X$ and $pp \rightarrow gs \rightarrow t\tilde{\ell}_i^- + X$ are equal, those two mutually conjugate processes have opposite A_t values as shown in Figs.15(c) and (d).

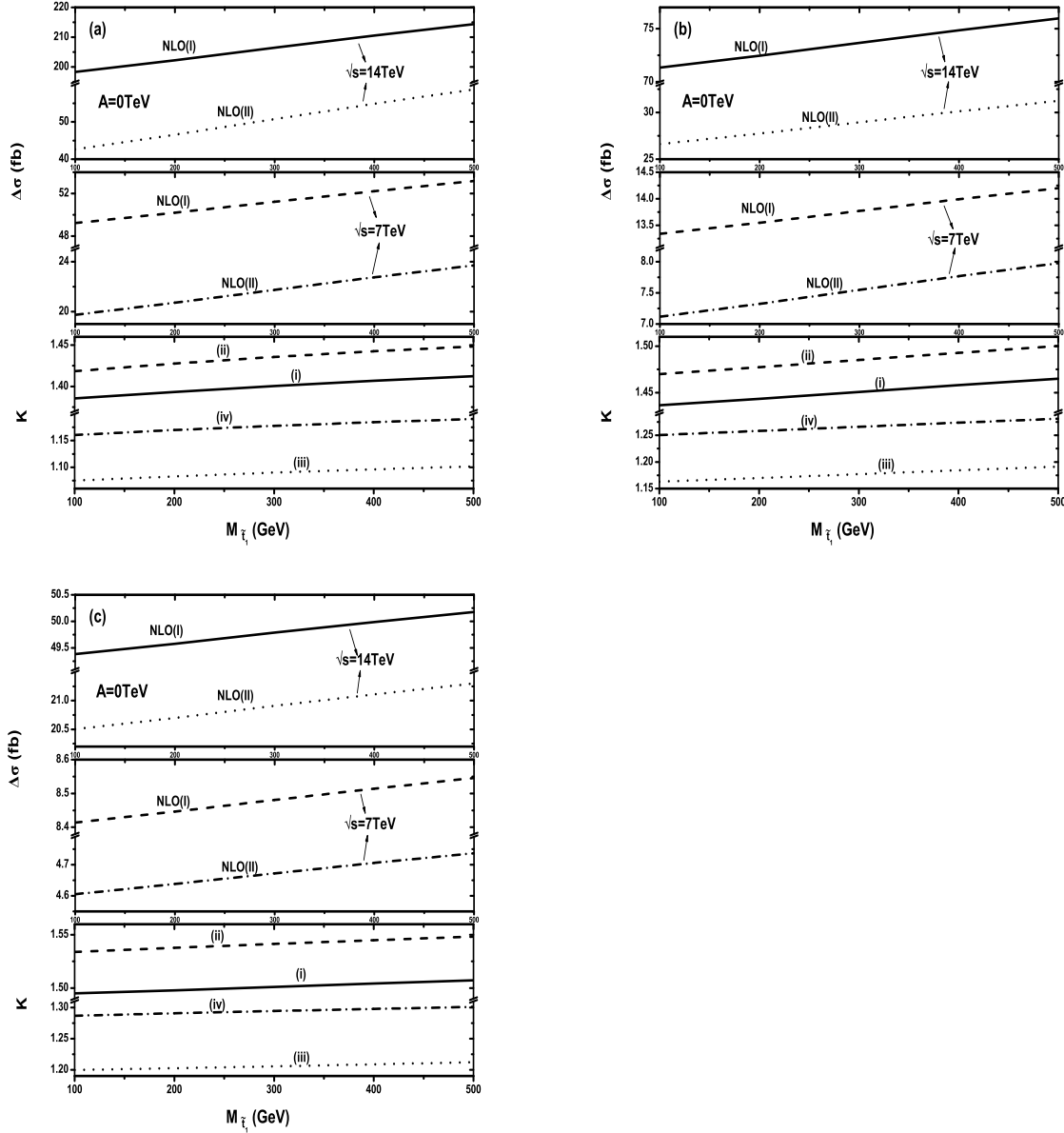


Figure 8: The NLO QCD correction to the LO cross sections ($\Delta\sigma_{NLO}$) and the corresponding K-factors versus $m_{\tilde{t}_1}$ with $A = 0 \text{ TeV}$ at the $\sqrt{s} = 7 \text{ TeV}$ and $\sqrt{s} = 14 \text{ TeV}$ LHC. (a) For the $pp \rightarrow gd \rightarrow t\tilde{\ell}_i^- + X$ process. (b) For the $pp \rightarrow g\bar{d} \rightarrow t\tilde{\ell}_i^+ + X$ process. (c) For the $pp \rightarrow gs \rightarrow t\tilde{\ell}_i^- + X$ process. The descriptions for the K-factor curves labeled (i), (ii), (iii) and (iv) are the same as in Figs.6.

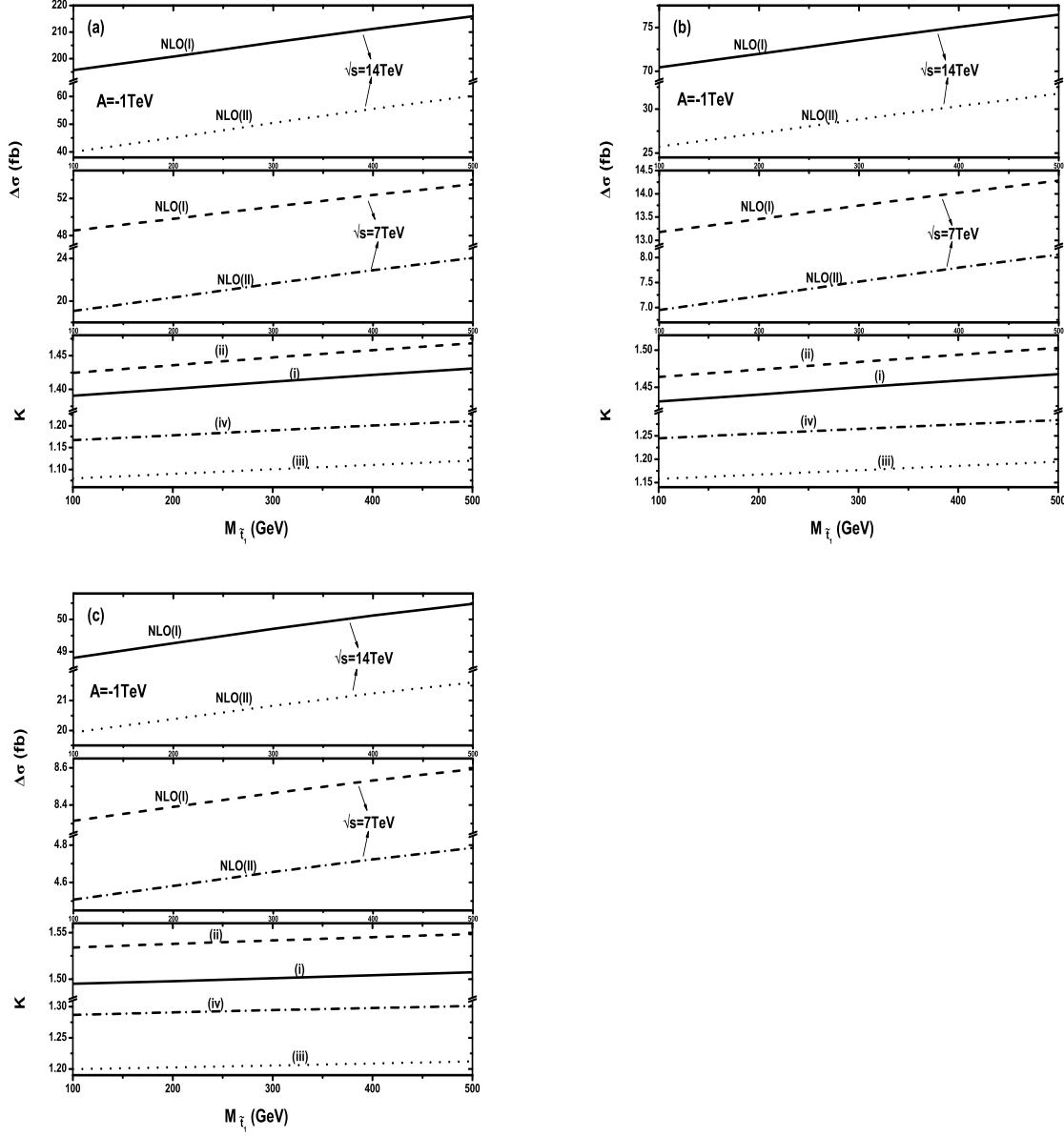


Figure 9: The NLO QCD correction to the LO cross sections ($\Delta\sigma_{NLO}$) and the corresponding K-factors versus $m_{\tilde{t}_1}$ with $A = -1 \text{ TeV}$ at the $\sqrt{s} = 7 \text{ TeV}$ and $\sqrt{s} = 14 \text{ TeV}$ LHC. (a) For the $pp \rightarrow gd \rightarrow t\tilde{\ell}_i^- + X$ process. (b) For the $pp \rightarrow g\bar{d} \rightarrow \bar{t}\tilde{\ell}_i^+ + X$ process. (c) For the $pp \rightarrow gs \rightarrow t\tilde{\ell}_i^- + X$ process. The descriptions for the K-factor curves labeled (i), (ii), (iii) and (iv) are the same as in Figs.6.

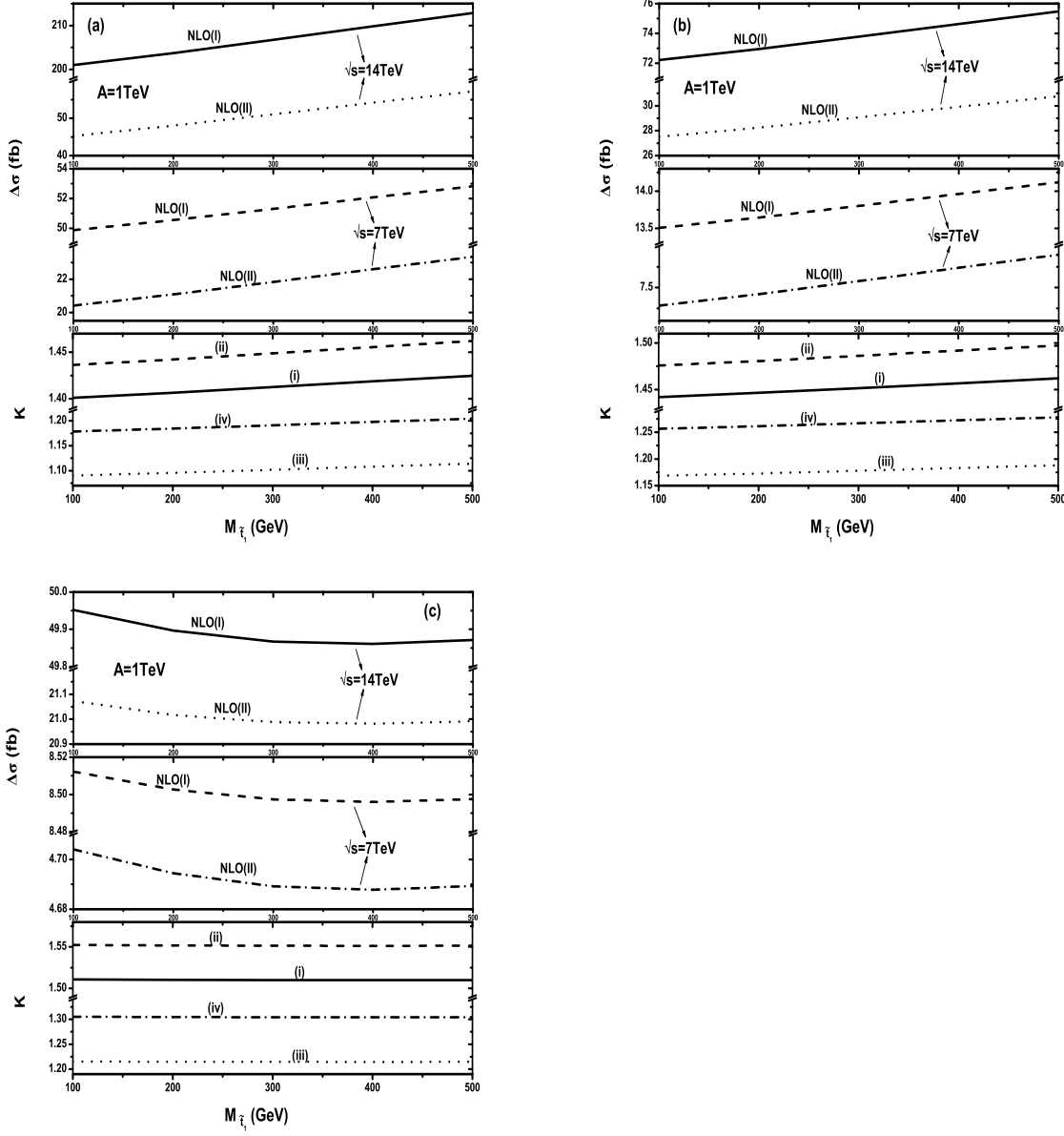


Figure 10: The NLO QCD correction to the LO cross sections ($\Delta\sigma_{NLO}$) and the corresponding K-factors versus $m_{\tilde{t}_1}$ with $A = 1$ TeV at the $\sqrt{s} = 7$ TeV and $\sqrt{s} = 14$ TeV LHC. (a) For the $pp \rightarrow gd \rightarrow t\tilde{l}_i + X$ process. (b) For the $pp \rightarrow g\bar{d} \rightarrow \tilde{t}\tilde{l}_i^+ + X$ process. (c) For the $pp \rightarrow gs \rightarrow t\tilde{l}_i + X$ process. The descriptions for the K-factor curves labeled (i), (ii), (iii) and (iv) are the same as in Figs.6.

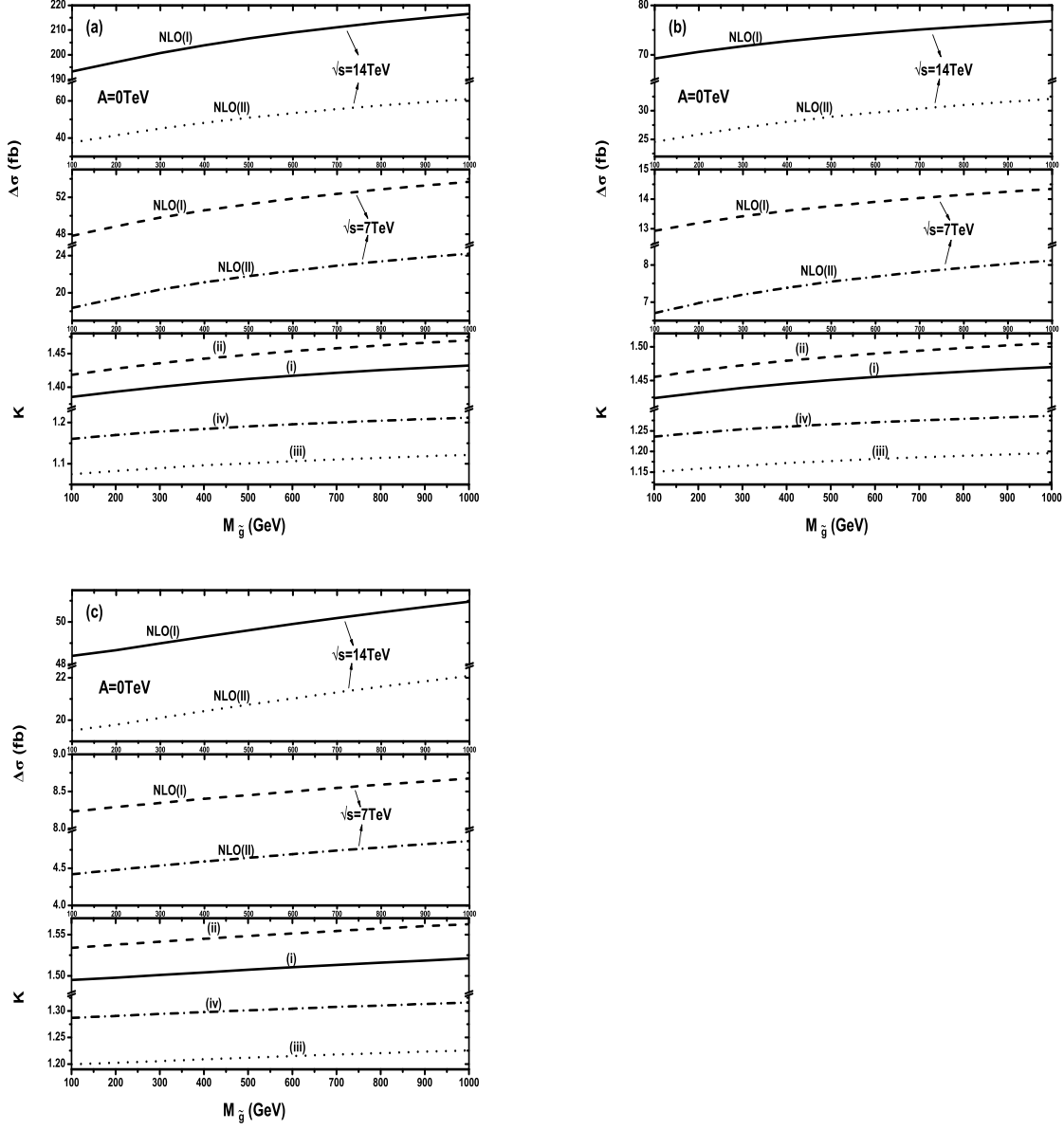


Figure 11: The NLO QCD correction to the LO cross sections ($\Delta\sigma_{NLO}$) and the corresponding K-factors versus $m_{\tilde{g}}$ with $A = 0 \text{ TeV}$ at the $\sqrt{s} = 7 \text{ TeV}$ and $\sqrt{s} = 14 \text{ TeV}$ LHC. (a) For the $pp \rightarrow gd \rightarrow t\tilde{\ell}_i^- + X$ process. (b) For the $pp \rightarrow g\bar{d} \rightarrow t\tilde{\ell}_i^+ + X$ process. (c) For the $pp \rightarrow gs \rightarrow t\tilde{\ell}_i^- + X$ process. The descriptions for the K-factor curves labeled (i), (ii), (iii) and (iv) are the same as in Figs.6.

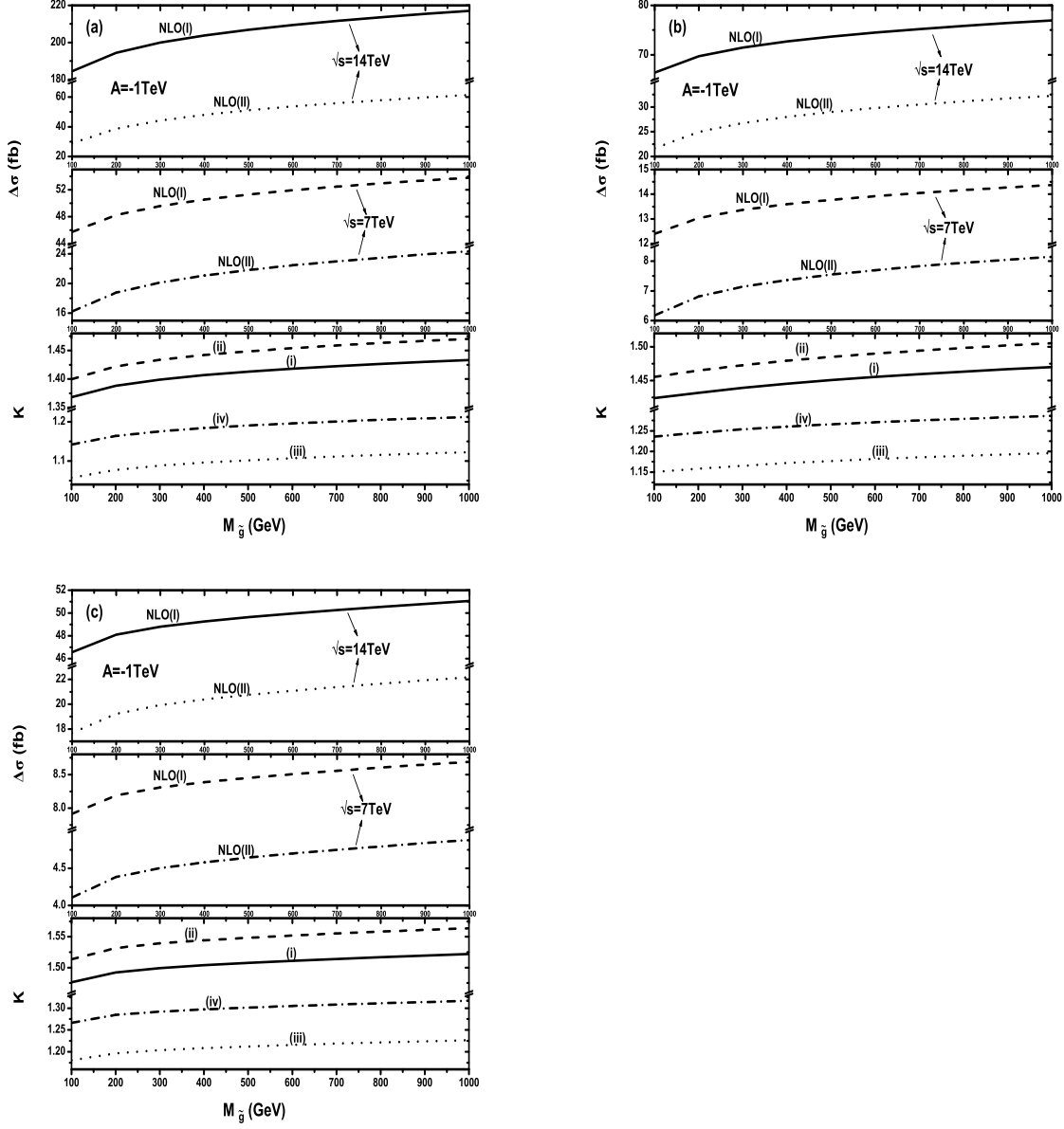


Figure 12: The NLO QCD correction to the LO cross sections ($\Delta\sigma_{NLO}$) and the corresponding K-factors versus $m_{\tilde{g}}$ with $A = -1 \text{ TeV}$ at the $\sqrt{s} = 7 \text{ TeV}$ and $\sqrt{s} = 14 \text{ TeV}$ LHC. (a) For the $pp \rightarrow g d \rightarrow t \tilde{\ell}_i^- + X$ process. (b) For the $pp \rightarrow g \bar{d} \rightarrow \bar{t} \tilde{\ell}_i^+ + X$ process. (c) For the $pp \rightarrow g s \rightarrow t \tilde{\ell}_i^- + X$ process. The descriptions for the K-factor curves labeled (i), (ii), (iii) and (iv) are the same as in Figs.6.

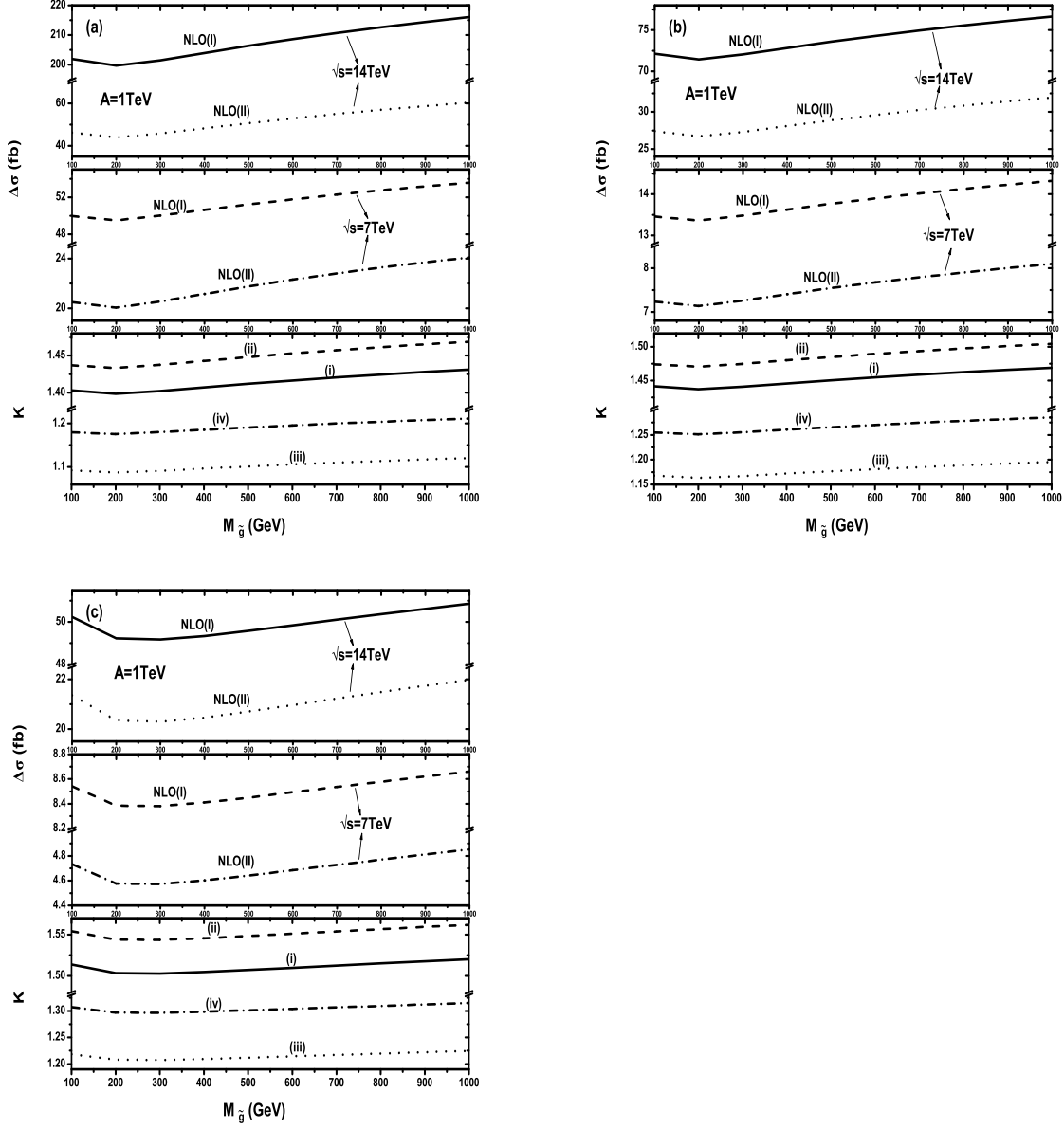


Figure 13: The NLO QCD correction to the LO cross sections ($\Delta\sigma_{NLO}$) and the corresponding K-factors versus $m_{\tilde{g}}$ with $A = 1 \text{ TeV}$ at the $\sqrt{s} = 7 \text{ TeV}$ and $\sqrt{s} = 14 \text{ TeV}$ LHC. (a) For the $pp \rightarrow gd \rightarrow t\tilde{\ell}_i^- + X$ process. (b) For the $pp \rightarrow g\bar{d} \rightarrow t\tilde{\ell}_i^+ + X$ process. (c) For the $pp \rightarrow gs \rightarrow t\tilde{\ell}_i^- + X$ process. The descriptions for the K-factor curves labeled (i), (ii), (iii) and (iv) are the same as in Figs.6.

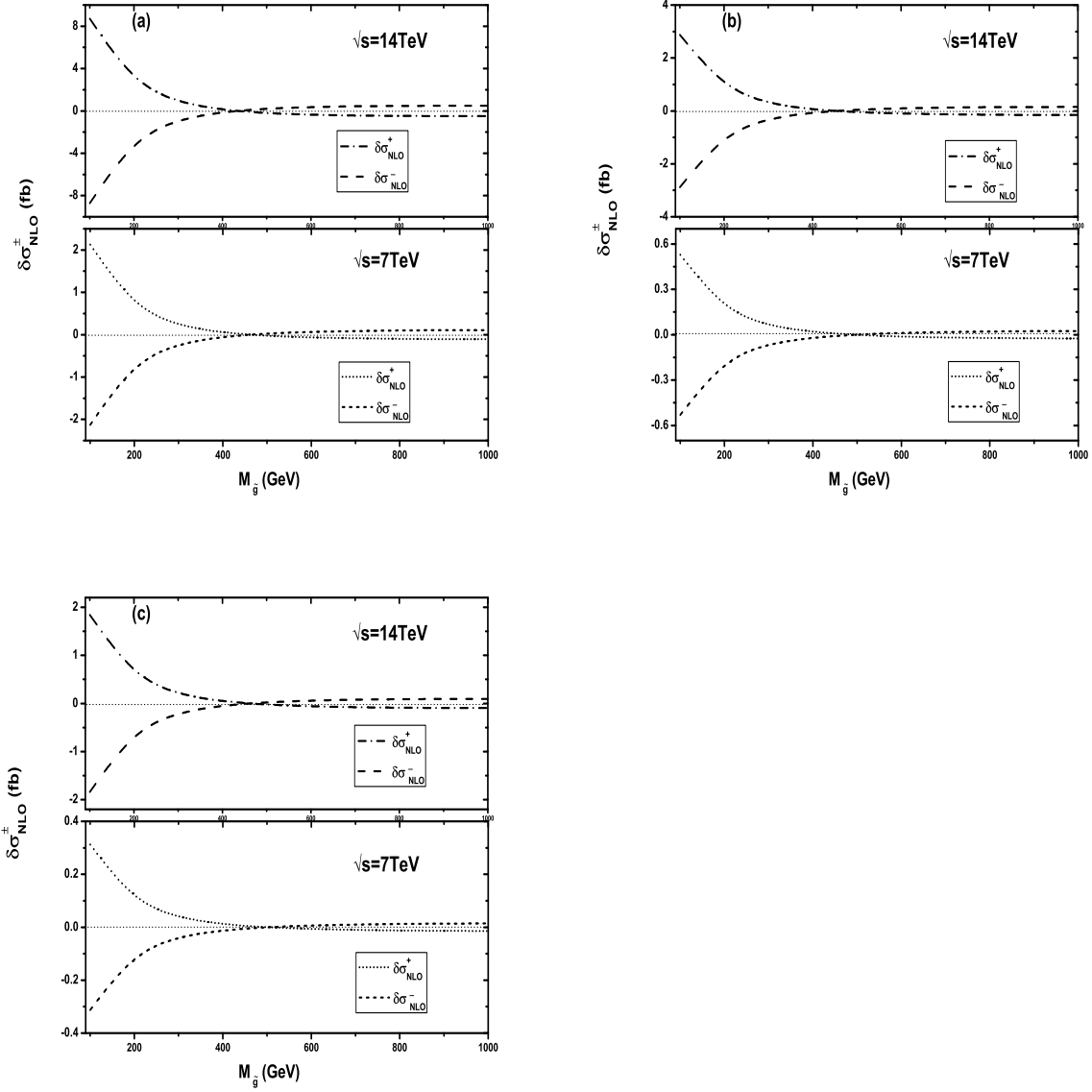


Figure 14: The difference between the NLO QCD corrections with $A = \pm 1 \text{ TeV}$ and $A = 0 \text{ TeV}$ versus $m_{\tilde{g}}$ at the $\sqrt{s} = 7 \text{ TeV}$ and $\sqrt{s} = 14 \text{ TeV}$ LHC. (a) For the $pp \rightarrow g d \rightarrow t \tilde{\ell}_i^- + X$ process. (b) For the $pp \rightarrow g \bar{d} \rightarrow t \tilde{\ell}_i^+ + X$ process. (c) For the $pp \rightarrow g s \rightarrow t \tilde{\ell}_i^- + X$ process.

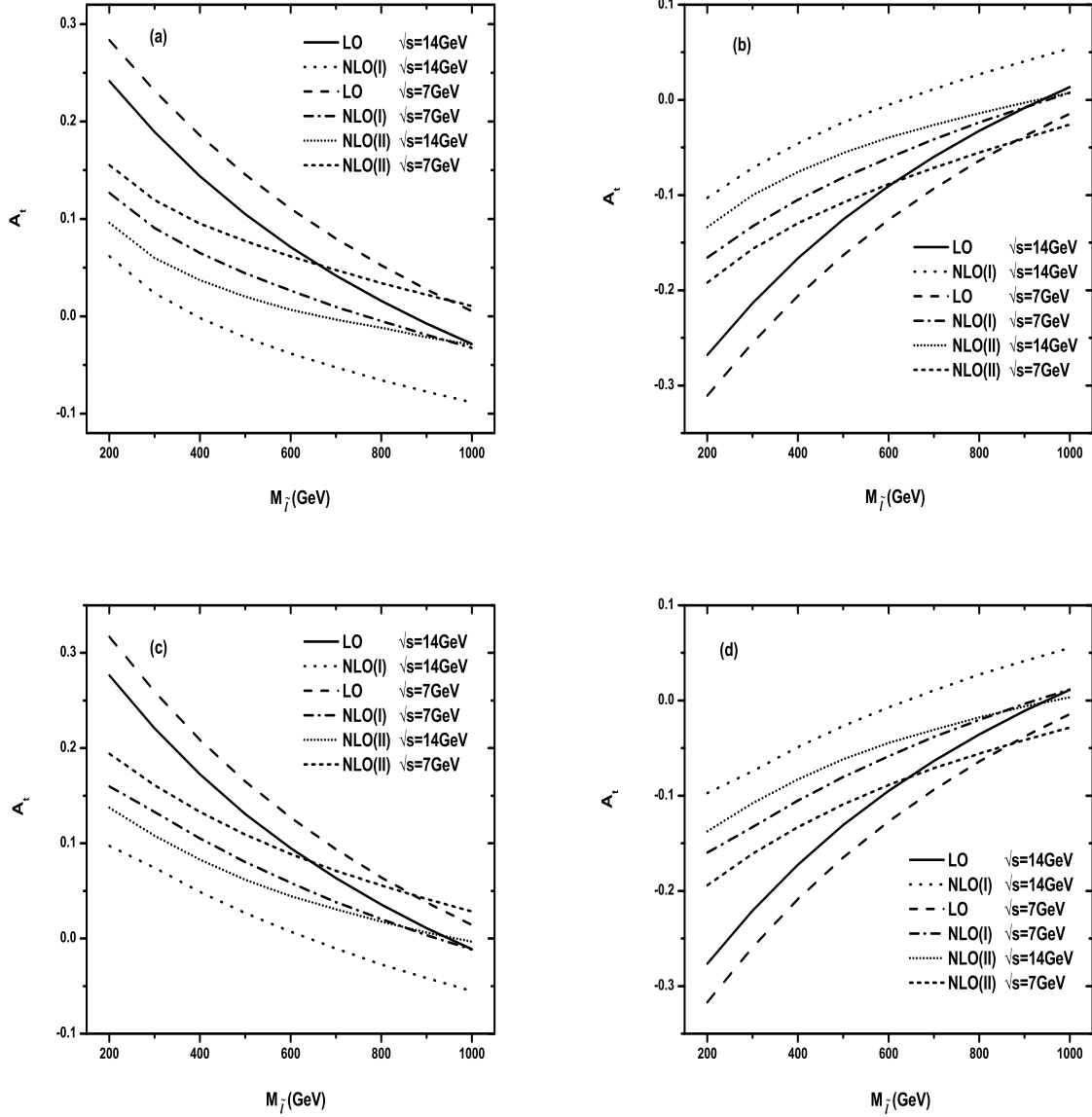


Figure 15: The LO and NLO QCD corrected polarization asymmetries (A_t) of the (anti)top quark at the early and future LHC as the functions of $m_{\tilde{t}_i}$ with $A = 0$ TeV. (a) For the process $pp \rightarrow gd \rightarrow t\tilde{\ell}_i^- + X$. (b) For the process $pp \rightarrow g\bar{d} \rightarrow \bar{t}\tilde{\ell}_i^+ + X$. (c) For the process $pp \rightarrow gs \rightarrow t\tilde{\ell}_i^- + X$. (d) For the process $pp \rightarrow g\bar{s} \rightarrow \bar{t}\tilde{\ell}_i^+ + X$.

In further discussion, we consider the case where $\tilde{\ell}_i^\pm = \tilde{\mu}^\pm$ (i.e., $i = 2$). After the production of the scalar muon, there follows a subsequential decay of $\tilde{\mu}^\pm \rightarrow \mu^\pm \tilde{\chi}_1^0$ with branch ratio 92.5% [31], then the final state involves muon, the lightest neutralino and (anti)top-quark jet ($\mu \tilde{\chi}_1^0 t(\bar{t})$). As a demonstration we assume there exist $m_{\tilde{\mu}} = 189.9 \text{ GeV}$, $\lambda'_{231} = 0.1$ and the other $\lambda' = 0$; then we present the LO, NLO QCD corrected transverse momentum distributions of the final (anti)top quark and the corresponding K-factors ($K(p_T^{t(\bar{t})}) = d\sigma_{NLO}(p_T^{t(\bar{t})})/d\sigma_{LO}(p_T^{t(\bar{t})})$) for the processes of $pp \rightarrow gd \rightarrow t\tilde{\mu}^- \rightarrow t\mu^- \tilde{\chi}_1^0 + X$ and $pp \rightarrow g\bar{d} \rightarrow \bar{t}\tilde{\mu}^+ \rightarrow \bar{t}\mu^+ \tilde{\chi}_1^0 + X$ at the LHC in Figs.16(a,b,c,d). Figs.16(a) and (c) are for the $p_T^t(p_T^{\bar{t}})$ distributions at the $\sqrt{s} = 14 \text{ TeV}$ LHC for the processes $pp \rightarrow gd \rightarrow t\mu^- \tilde{\chi}_1^0 + X$ and $pp \rightarrow g\bar{d} \rightarrow \bar{t}\mu^+ \tilde{\chi}_1^0 + X$, respectively, and Figs.16(b) and (d) are at the $\sqrt{s} = 7 \text{ TeV}$ LHC for the processes $pp \rightarrow gd \rightarrow t\mu^- \tilde{\chi}_1^0 + X$ and $pp \rightarrow g\bar{d} \rightarrow \bar{t}\mu^+ \tilde{\chi}_1^0 + X$, respectively. These figures show that in Figs.16 there exist peaks located at the position around $p_T^t(p_T^{\bar{t}}) \sim 80 \text{ GeV}$ at the early and future LHC, separately. We can see that the LO differential cross sections are significantly enhanced by the QCD corrections with inclusive jet selection scheme, while the QCD correction by using an exclusive jet selection scheme keeps the convergence of the perturbative series in the plotted $p_T^t(p_T^{\bar{t}})$ range.

The transverse momentum distributions of the final muon and the lightest neutralino, and the corresponding K-factors for the $pp \rightarrow gd \rightarrow t\mu^- \tilde{\chi}_1^0 + X$ process at the $\sqrt{s} = 14 \text{ TeV}$ LHC are depicted in Figs.17(a,b), separately, while the corresponding distributions and K-factors at the $\sqrt{s} = 7 \text{ TeV}$ LHC are depicted in Figs.17(c,d), respectively. In Figs.18(a,b,c,d) we show the transverse momentum distributions and the corresponding K-factors of the final particles after the decay of $\tilde{\mu}^+$ for the process $pp \rightarrow g\bar{d} \rightarrow \bar{t}\mu^+ \tilde{\chi}_1^0 + X$. Figs.18(a) and (b) show the p_T distributions of the final μ and $\tilde{\chi}_1^0$ and K-factors at the $\sqrt{s} = 14 \text{ TeV}$ LHC, separately, and Figs.18(c) and (d) demonstrate the p_T^μ and $p_T^{\tilde{\chi}_1^0}$ distributions and K-factors at the $\sqrt{s} = 7 \text{ TeV}$ LHC respectively. In the calculation for these results we use the narrow-width approximation (NWA) method to handle the resonant scalar muon effect. Here we assume $\lambda'_{231} = 0.1$ and the other $\lambda' = 0$. The curves of K-factor labeled (I) and (II) correspond to adopting the inclusive and exclusive gluon/(anti)quark jet event selection schemes, respectively. It is clear that with the exclusive jet event selection scheme we can keep the convergence of the perturbative series,

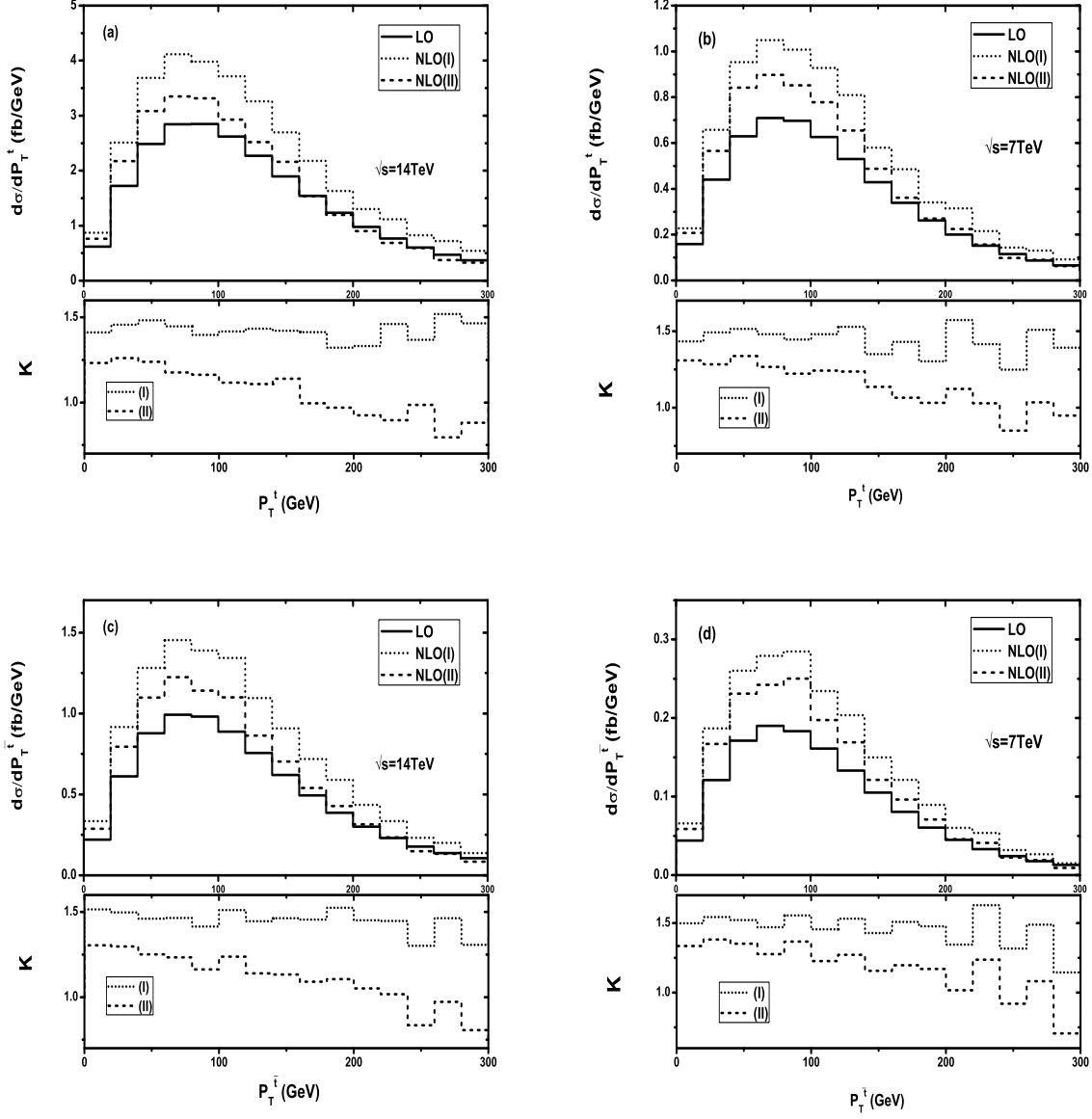


Figure 16: The LO, NLO QCD corrected differential cross sections of the transverse momentum of final (anti)top quark and the corresponding K-factors $K(p_T^{t(i)}) = d\sigma_{NLO}(p_T^{t(i)})/d\sigma_{LO}(p_T^{t(i)})$ with $A = 0$ TeV. (a) For the process $pp \rightarrow gd \rightarrow t\tilde{\ell}_i^- + X$ at the $\sqrt{s} = 14$ TeV LHC. (b) For the process $pp \rightarrow gd \rightarrow t\tilde{\ell}_i^- + X$ at the $\sqrt{s} = 7$ TeV LHC. (c) For the process $pp \rightarrow g\bar{d} \rightarrow \bar{t}\tilde{\ell}_i^+ + X$ at the $\sqrt{s} = 14$ TeV LHC. (d) For the process $pp \rightarrow g\bar{d} \rightarrow \bar{t}\tilde{\ell}_i^+ + X$ at the $\sqrt{s} = 7$ TeV LHC. The curves of K-factor labeled (I) and (II) correspond to adopting the inclusive and exclusive scheme, respectively.

process	$\sigma_{LO}(\text{fb})$	$p_{T,jet}^{cut} = 50\text{GeV}, \eta_{jet}^{cut} = 3$		$p_{T,jet}^{cut} = 35\text{GeV}, \eta_{jet}^{cut} = 2.7$	
		$\sigma_{NLO}(\text{fb})$	K-factor	$\sigma_{NLO}(\text{fb})$	K-factor
$pp \rightarrow gd \rightarrow t\tilde{\ell}_i^- + X$	501.0(1)/114.34(2)	541.4(4)/134.9(2)	1.081/1.180	491.9(4)/123.6(1)	0.982/1.081
$pp \rightarrow gd \rightarrow \bar{t}\tilde{\ell}_i^+ + X$	163.4(2)/28.39(4)	184.7(4)/36.08(9)	1.130/1.271	169.7(3)/33.03(8)	1.038/1.164
$pp \rightarrow gs \rightarrow t\tilde{\ell}_i^- + X$	97.78(1)/15.411(2)	115.9(2)/19.85(9)	1.185/1.288	106.4(2)/18.07(8)	1.089/1.172

Table 3: The numerical results of the LO and NLO QCD corrected total cross sections by adopting the exclusive selection scheme for the $pp \rightarrow gd \rightarrow t\tilde{\ell}^- + X$, $pp \rightarrow g\bar{d} \rightarrow \bar{t}\tilde{\ell}^+ + X$ and $pp \rightarrow gs \rightarrow t\tilde{\ell}_i^- + X$ processes with $A = 0 \text{ TeV}$. The data on the left and right sides of the slash correspond to the results for $\sqrt{s} = 14 \text{ TeV}$ and $\sqrt{s} = 7 \text{ TeV}$, respectively. There we take $m_{\tilde{\ell}_i} = 189.9 \text{ GeV}$.

and the NLO QCD corrections mostly enhance the LO differential cross sections of the final particles in the plotted p_T range.

In Table 3 we list some of the numerical results for the LO and NLO QCD corrected total cross sections by adopting the exclusive gluon/light-(anti)quark jet selection scheme for the $pp \rightarrow gd \rightarrow t\tilde{\ell}_i^- + X$, $pp \rightarrow g\bar{d} \rightarrow \bar{t}\tilde{\ell}_i^+ + X$ and $pp \rightarrow gs \rightarrow t\tilde{\ell}_i^- + X$ processes at the $\sqrt{s} = 14 \text{ TeV}$ and 7 TeV LHC. There we take $m_{\tilde{\ell}_i} = 189.9 \text{ GeV}$, $\lambda'_{i31} = 0.1$ and the other $\lambda' = 0$ for the first two processes, $\lambda'_{i32} = 0.1$ and the other $\lambda' = 0$ for the last process. We consider the phase space with the restriction of either $p_T^{jet} < p_{T,jet}^{cut} = 35, 50 \text{ GeV}$ or $\eta^{jet} > \eta_{jet}^{cut} = 2.7, 3$ for gluon/light-(anti)quark jet transverse momentum.

IV. Summary

In this paper, we calculate the complete NLO QCD corrections to the single slepton associated with a (anti)top-quark production process at the early ($\sqrt{s} = 7 \text{ TeV}$) and future ($\sqrt{s} = 14 \text{ TeV}$) LHC. We investigate the dependence of the LO and the NLO QCD integrated cross sections on the factorization/renormalization energy scale, and study the influence of slepton, stop-quark and gluino masses on the NLO QCD corrected cross sections. We point out that the uncertainty of the LO cross section due to the introduced energy scale μ is apparently improved by including NLO QCD corrections, and the exclusive jet event selection scheme keeps the convergence of

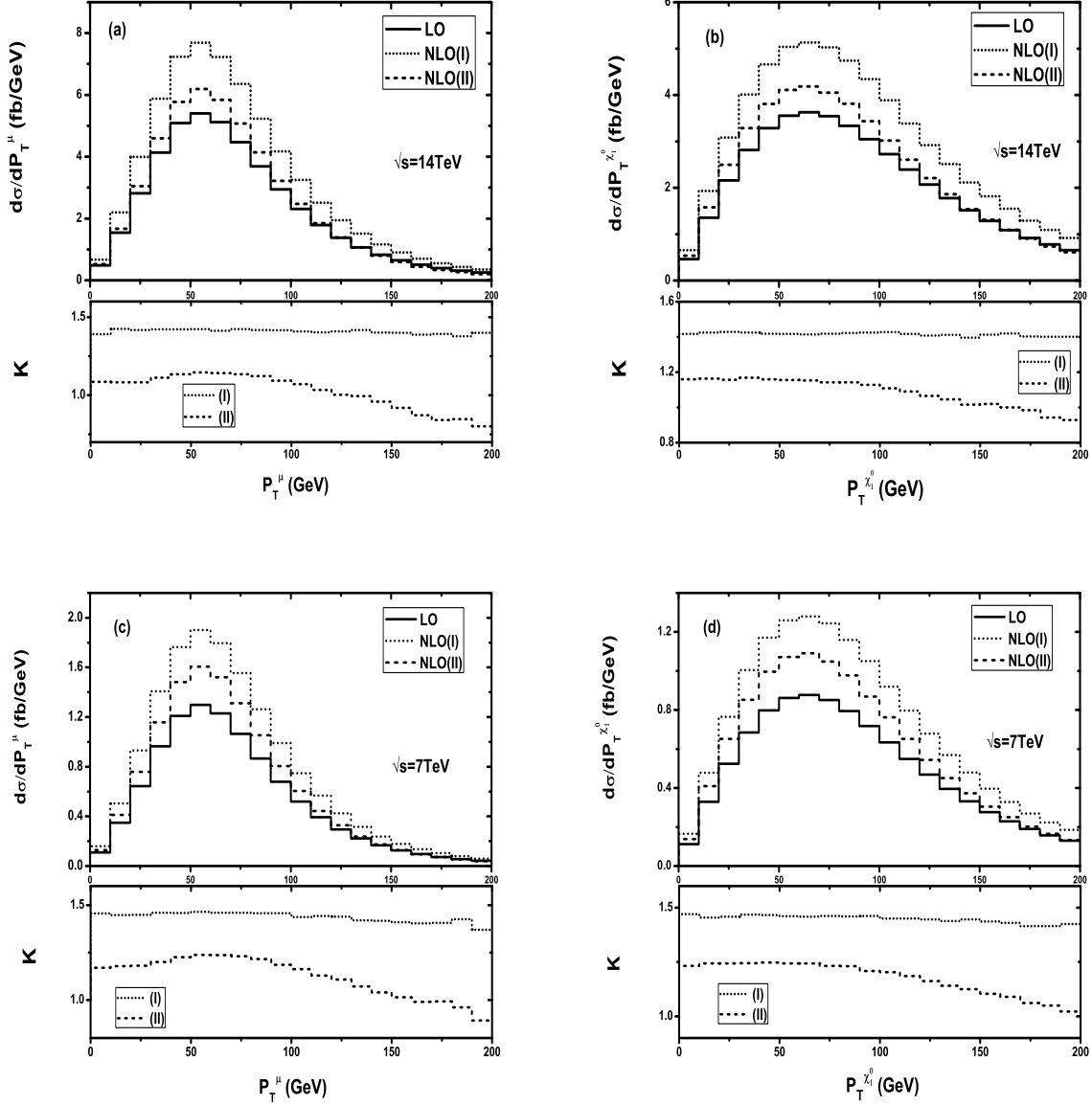


Figure 17: The LO, NLO QCD corrected distributions of the transverse momenta of final muon and neutralino for the process $pp \rightarrow gd \rightarrow t\mu^- \tilde{\chi}_1^0 + X$, and the corresponding K-factors ($K(p_T) \equiv \frac{d\sigma_{NLO}}{dp_T} / \frac{d\sigma_{LO}}{dp_T}$) with $A = 0 \text{ TeV}$ at the LHC. (a) For the final muon at the $\sqrt{s} = 14 \text{ TeV}$ LHC. (b) For the final $\tilde{\chi}_1^0$ at the $\sqrt{s} = 14 \text{ TeV}$ LHC. (c) For the final muon at the $\sqrt{s} = 7 \text{ TeV}$ LHC. (d) For the final $\tilde{\chi}_1^0$ at the $\sqrt{s} = 7 \text{ TeV}$ LHC.

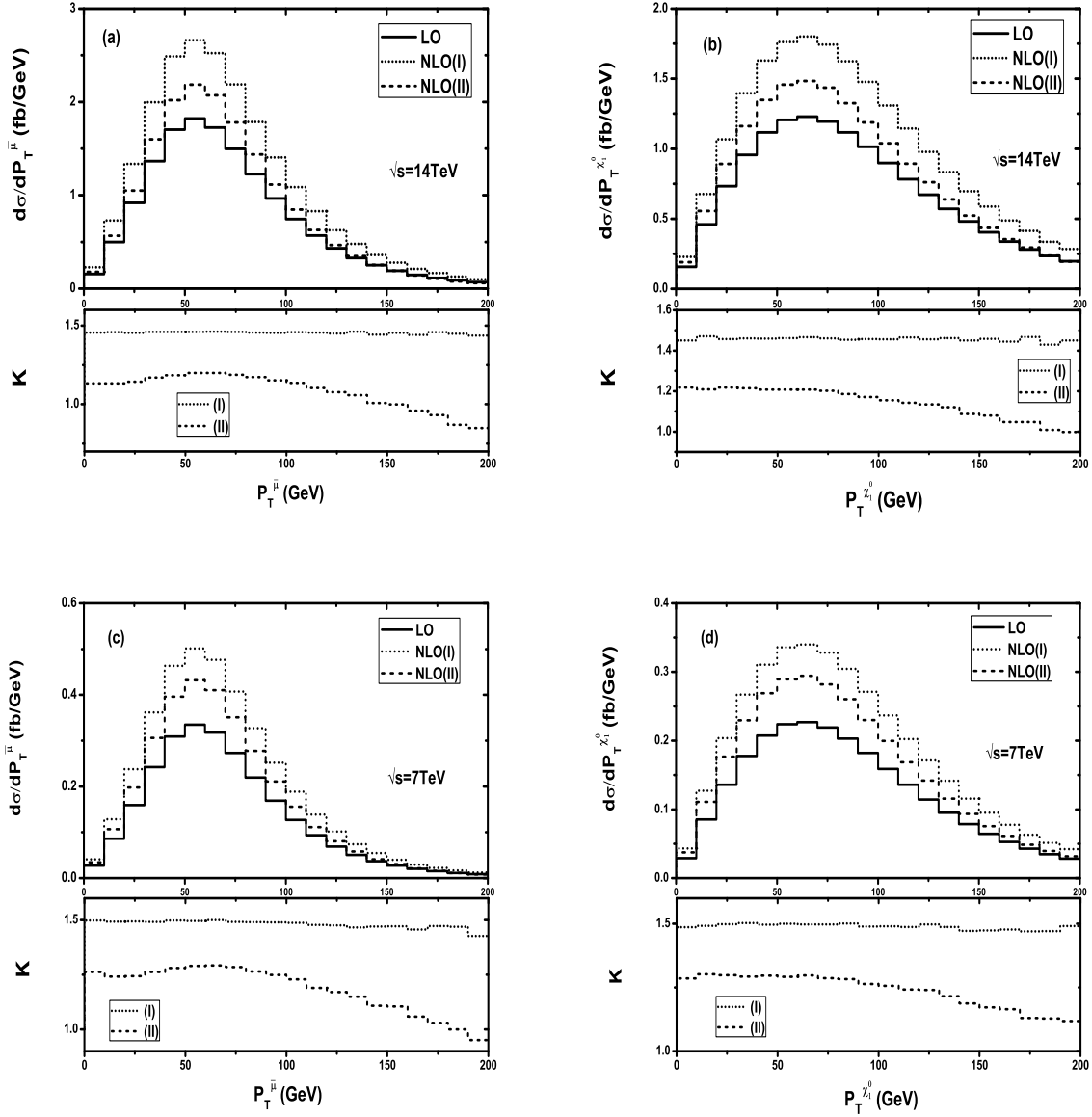


Figure 18: The LO, NLO QCD corrected distributions of the transverse momenta and the corresponding K-factors ($K(p_T) \equiv \frac{d\sigma_{NLO}}{dp_T} / \frac{d\sigma_{LO}}{dp_T}$) of the final particles for the process $pp \rightarrow g\bar{d} \rightarrow \bar{t}\mu^+\tilde{\chi}_1^0 + X$ with $A = 0$ TeV at the LHC. (a) For final muon at the $\sqrt{s} = 14$ GeV LHC. (b) For the final $\tilde{\chi}_1^0$ at the $\sqrt{s} = 14$ GeV LHC. (c) For the final muon at the $\sqrt{s} = 7$ GeV LHC. (d) For the final $\tilde{\chi}_1^0$ at the $\sqrt{s} = 7$ GeV LHC.

the perturbative calculations better than the inclusive scheme. We find also that the SUSY QCD correction generally increases if the \tilde{t}_1 or \tilde{g} mass is getting large, but the non-zero \tilde{t}_j - \tilde{d}_k - \tilde{l}_i coupling with $A = 1 \text{ TeV}$ could distort that curve tendency in some cases. We present the LO and the QCD corrected distributions of the transverse momenta of final products involving (anti)top quark, muon and the lightest neutralino. Our results show that the NLO QCD corrections suppress the polarization asymmetries of final (anti)top quark, and mostly enhance the transverse momentum distributions of final particles.

Acknowledgments: This work was supported in part by the National Natural Science Foundation of China (Contract No.10875112, No.11075150, No.11005101), and the Specialized Research Fund for the Doctoral Program of Higher Education (Contract No.20093402110030).

References

- [1] P. Fayet, Phys. Lett. B **69**, 489 (1977)
- [2] G.R. Farrar, P. Fayet, Phys. Lett. B **76**, 575 (1978)
- [3] L.E. Ibanez, G.G. Ross, Nucl. Phys. B **368**, 3 (1992)
- [4] S. Weinberg, Phys. Rev. D **26**, 287 (1982)
- [5] N. Sakai, T. Yanagida, Nucl. Phys. B **197**, 533 (1982)
- [6] R. Barbier, C. Berat, M. Besancon, M. Chemtob, A. Deandrea, E. Dudas, P. Fayet, S. Lavignac, G. Moreau, E. Perez, Y. Sirois, Phys. Rept. **420**, 1-202 (2005). [arXiv:hep-ph/0406039]
- [7] J.J. Cao, Z.X. Heng, L. Wu, J.M. Yang, Phys. Rev. D **79**, 054003 (2009)
- [8] T.M.P. Tait, C.-P. Yuan, Phys. Rev. D **63**, 014018 (2000)
- [9] R. Barbier et al., Phys. Rep. **420**, 1 (2005). [arXiv:hep-ph/0406039]

- [10] P. Chiappetta, A. Deandrea, E. Nagy, S. Negroni, G. Polesello, J.M. Virey, Phys. Rev. D **61**, 115008 (2000). [arXiv:hep-ph/9910483]
- [11] F. Borzumati, J. L. Kneur and N. Polonsky, Phys. Rev. D **60** 115011 (1999). [arXiv:hep-ph/9905443]
- [12] Z.H. Yu, P. Herbert, W.G. Ma, L. Han, Y. Jiang, Eur. Phys. J. C **16**, 695 (2000). [arXiv:hep-ph/9910323]
- [13] M. Chaichian, K. Huitu, Z.H. Yu, Phys. Lett. B **490** 87 (2000). [arXiv:hep-ph/0007220]
- [14] H. Zhou, W.G. Ma, Y. Jiang, R.Y. Zhang, L.H. Wan, Phys. Rev. D **64** 095006 (2001)
- [15] R.J. Oakes, K. Whisnant, J.M. Yang, B.-L. Young, X. Zhang, Phys. Rev. D **57**, 534-540 (1998)
- [16] A. Datta, J.M. Yang, B.-L. Young, X. Zhang, Phys. Rev. D **56**, 3107-3113 (1997)
- [17] M. Arai, K. Huitu, S.K. Rai, K. Rao, J. High Energy Phys. **1008**, 082 (2010)
- [18] M.A. Bernhardt, H.K. Dreiner, S. Grab and P. Richardson, Phys. Rev. D **78**, 015016 (2008)
- [19] T. Hahn, Comput. Phys. Commun. **140**, 418 (2001)
- [20] T. Hahn, M. Perez-Victoria, Comput. Phys. Commun. **118**, 153 (1999)
- [21] F. Borzumati, J.S. Lee, Phys. Rev. D **66**, 115012 (2002)
- [22] A. Denner, Fortschr. Phys. **41**, 307 (1993)
- [23] W.J. Marciano, Phys. Rev. D **29**, 580 (1984)
- [24] W.J. Marciano, Phys. Rev. D **31**, 213 (1984) (E)
- [25] T. Kinoshita, J. Math. Phys. **3**, 650 (1962)
- [26] T.D. Lee, M. Nauenberg, Phys. Rev. B **133**, 1549 (1964)

- [27] B.W. Harris, J.F. Owens, Phys. Rev. D **65**, 094032 (2002). hep-ph/0102128
- [28] J. Pumplin, et al., J. High Energy Phys. **0207**, 012 (2002)
- [29] D. Stump, et al., J. High Energy Phys. **0310**, 046 (2003)
- [30] C. Amsler, et al., Phys. Lett. B **667**, 1 (2008)
- [31] J.A. Aguilar-Saavedra, et al., Eur. Phys. J. C **46**, 43 (2006)
- [32] <http://www.phys.ufl.edu/~jblender/isajet/isajet.html>
- [33] H.K. Dreiner, S. Grab, M. Kramer, M.K. Trenkel, Phys. Rev. D **75**, 035003 (2007).
[arXiv:hep-ph/0611195]